NASA/CR-2003-212678

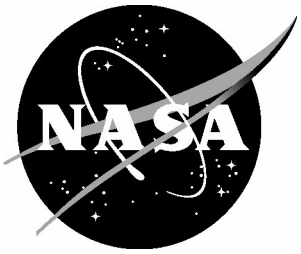

Photogrammetry and Videogrammetry Methods Development for Solar Sail Structures

Jonathan T. Black
Joint Institute for Advancement of Flight Sciences
Langley Research Center, Hampton, Virginia

December 2003

The NASA STI Program Office . . . in Profile

Since its founding, NASA has been dedicated to the advancement of aeronautics and space science. The NASA Scientific and Technical Information (STI) Program Office plays a key part in helping NASA maintain this important role.

The NASA STI Program Office is operated by Langley Research Center, the lead center for NASA's scientific and technical information. The NASA STI Program Office provides access to the NASA STI Database, the largest collection of aeronautical and space science STI in the world. The Program Office is also NASA's institutional mechanism for disseminating the results of its research and development activities. These results are published by NASA in the NASA STI Report Series, which includes the following report types:

- TECHNICAL PUBLICATION. Reports of completed research or a major significant phase of research that present the results of NASA programs and include extensive data or theoretical analysis. Includes compilations of significant scientific and technical data and information deemed to be of continuing reference value. NASA counterpart of peer-reviewed formal professional papers, but having less stringent limitations on manuscript length and extent of graphic presentations.

- TECHNICAL MEMORANDUM. Scientific and technical findings that are preliminary or of specialized interest, e.g., quick release reports, working papers, and bibliographies that contain minimal annotation. Does not contain extensive analysis.

- CONTRACTOR REPORT. Scientific and technical findings by NASA-sponsored contractors and grantees.

- CONFERENCE PUBLICATION. Collected papers from scientific and technical conferences, symposia, seminars, or other meetings sponsored or co-sponsored by NASA.

- SPECIAL PUBLICATION. Scientific, technical, or historical information from NASA programs, projects, and missions, often concerned with subjects having substantial public interest.

- TECHNICAL TRANSLATION. English-language translations of foreign scientific and technical material pertinent to NASA's mission.

Specialized services that complement the STI Program Office's diverse offerings include creating custom thesauri, building customized databases, organizing and publishing research results ... even providing videos.

For more information about the NASA STI Program Office, see the following:

- Access the NASA STI Program Home Page at ***http://www.sti.nasa.gov***

- E-mail your question via the Internet to help@sti.nasa.gov

- Fax your question to the NASA STI Help Desk at (301) 621-0134

- Phone the NASA STI Help Desk at (301) 621-0390

- Write to:
  NASA STI Help Desk
  NASA Center for AeroSpace Information
  7121 Standard Drive
  Hanover, MD 21076-1320

NASA/CR-2003-212678

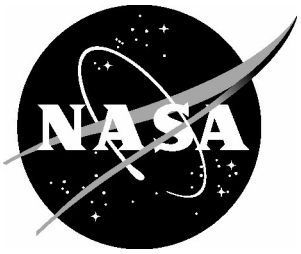

Photogrammetry and Videogrammetry Methods Development for Solar Sail Structures

Jonathan T. Black
Joint Institute for Advancement of Flight Sciences
Langley Research Center, Hampton, Virginia

National Aeronautics and
Space Administration

Langley Research Center
Hampton, Virginia 23681-2199

Prepared for Langley Research Center
under Cooperative Agreement NCC1-03008

December 2003

Available from:

NASA Center for AeroSpace Information (CASI)
7121 Standard Drive
Hanover, MD 21076-1320
(301) 621-0390

National Technical Information Service (NTIS)
5285 Port Royal Road
Springfield, VA 22161-2171
(703) 605-6000

ABSTRACT

Responding to recent advances in materials manufacturing, specifically membrane production, the space community has begun to focus considerable attention on gossamer technologies as a means of reducing launch costs and volumes. Ultra-lightweight and inflatable gossamer space structures are designed to be tightly packaged for launch, then deploy or inflate once in space. These properties will allow for in-space construction of very large structures 10 to 100 meters in size such as solar sails, inflatable antennae, and space solar power stations using a single launch. Solar sails are perhaps the most studied of the gossamer technologies because of the propellantless propulsion they provide. Gossamer structures do, however, have significant complications. Their low mass and high flexibility characteristics make them difficult to test on the ground. The added mass and stiffness of attached measurement devices can significantly alter the static and dynamic properties of the structure, necessitating an alternative approach for characterization.

This report discusses the development and application of metrology methods called photogrammetry and videogrammetry that make accurate measurements from photographs. These methods have been adapted for the static and dynamic characterization of gossamer structures, as four specific solar sail applications demonstrate. The applications prove that high-resolution, full-field, non-contact static measurements of solar sails using dot projection photogrammetry are possible as well as full-field, non-contact, dynamic characterization using dot projection videogrammetry. The accuracy of the measurement of the resonant frequencies and operating deflection shapes that were extracted surpassed expectations. While other non-contact measurement methods exist, they are not full-field and require significantly more time to take data.

ACKNOWLEDGEMENTS

The author would like to thank Dr. Keith Belvin, Dr. Kara Slade, Mr. Tom Jones, Dr. Adrian Dorrington, Dr. Paul Danehy, and all the members of the Ultra-lightweight and Inflatable Structures group at NASA Langley Research Center (LaRC) for their commitment to excellence and their drive to explore, the members of the Structural Dynamics Branch at LaRC for their hospitality, Prof. Robert Blanchard of George Washington University for his guidance, Dr. Jack Leifer of the University of Kentucky and Dr. Joe Blandino of James Madison University for their collaboration and creativity, his thesis advisor Dr. Paul Cooper of George Washington University for his direction, thesis committee member Prof. Robert Sandusky of George Washington University, and his friends and family for their love and support.

The author would especially like to thank his NASA advisor, Mr. Richard Pappa of LaRC whose kindness, generosity, and devotion have made working at NASA an edifying and broadening experience. He has taught me more than I ever could have imagined and my gratitude runs deeper than I ever could express.

TABLE OF CONTENTS

LIST OF FIGURES

LIST OF TABLES

1. INTRODUCTION

The average cost to place a payload into low earth orbit aboard a U.S. expendable launch vehicle is approximately $20,000 per kilogram with payload size restricted to approximately 65 cubic meters. Visionary plans within the government and private sector call for deploying large spacecraft with huge apertures, sun shields, and solar arrays; spacecraft with prohibitively high launch and assembly costs using traditional methods of construction. For such satellites to be feasible, a new class of structures using gossamer technology is under development. This unique technology uses ultra-thin membranes and inflatable booms to reduce launch volumes by a factor of 50 and launch mass by a factor of 10. Gossamer structures will not only fly as satellite components, but also as stand-alone spacecraft. Solar sails will be among the first to demonstrate the full potential of gossamer technology [1-8]

1.1 Measurement Methods

Photogrammetry is the science of making accurate shape measurements from photographs [9]. Using high contrast retro-reflective targets, static shape characterizations of gossamer test articles, such as inflatable antennae, have been achieved in previous work at the NASA Langley Research Center (LaRC) [10-13]. Videogrammetry expands the methods and techniques of close-range photogrammetry and applies them to a sequence of images to generate a series of the 3-D models produced with standard photogrammetry. The models are then linked to create dynamic data for such tasks as modal analysis and deployment tracking. Attached retro-reflective targets, however, may alter the static and dynamic behavior of the membranes. Therefore, to effectively measure ultra-thin membranes without physically attaching targets, totally

non-contact projected circular targets were used in conjunction with photogrammetry [14, 15].

1.2 Objective

Current solar sail development at LaRC is focused in three areas: materials development, analytical model development and validation, and experimental methods. The techniques developed here apply to the second and third research areas. High quality structural analytical models require highly accurate, high-resolution measurements of solar sail test articles for validation. Non-contact, full-field measurements of this nature have never before been achieved with sufficient resolution and quality to adequately perform this task. This report details the development of non-contact photogrammetric and videogrammetric methods for use on Earth and potentially in space for the static and dynamic characterization of solar sails. Also included are an analysis of the accuracy and precision of the methods, a discussion of the hardware and its effects on the final results, strengths and weaknesses of the methods, and suggestions for future work.

2. GOSSAMER STRUCTURES

The term *gossamer* is generally applied to ultra-low-mass space structures. Frequently these structures are designed to be tightly packaged for launch, and then to deploy or inflate once in space. These properties will enable construction of a variety of structures that are impractical using current space hardware. Solar sails in particular have been the focus of many research and development efforts because of the unique propulsion they provide.

2.1 Overview

Most gossamer space structures rely on ultra-thin membranes and inflatable tubes to achieve a reduction compared to standard space hardware in launch mass by as much as 10 times and in launch volume by as much as 50 times. The technology has been adapted for possible use in a wide variety of applications, including deployable ballutes for aerobraking on Mars, telescope sunshields, and membrane space solar arrays. Solar sails are another gossamer application receiving considerable research and development funding at NASA and are discussed in the following section. [1, 3-6, 8, 16]

In addition to satellite components, research into stand-alone gossamer spacecraft has progressed and can be categorized based on structure size, shown in Figure 1 below. Inflatable apertures include telescopes and antennae from 10 to 70 meters in diameter, solar sails range from 70 to 200 meters per side, and space solar power stations may be up to square kilometers in size. These spacecraft will serve many purposes, including studying planets orbiting distant stars, propelling satellites on inter-stellar voyages, and providing clean energy on Earth [4, 6].

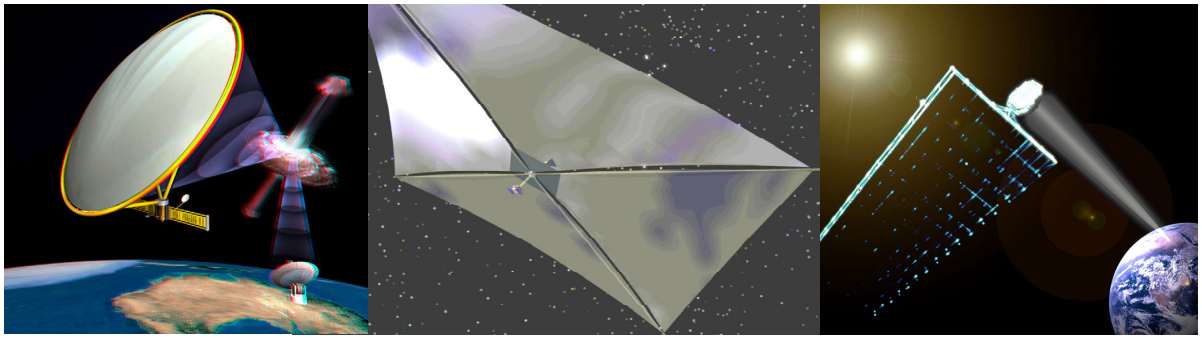

(a) Inflatable apertures 10's m (b) Solar sails 100's m (c) Space solar power arrays 1 km

Figure 1 – Gossamer structures

Results have been so promising, in fact, that several NASA missions planned for the next decade, including the GEOStorm solar sail mission and the James Webb Space Telescope (Figure 2), as well as more long-range possibilities such as a Mercury sample return, will make use of membrane structures up to hundreds of square meters in size [1, 4-7, 17, 18]. Missions of this type are impossible today using traditional space hardware due to the complexity, time, weight restrictions, and high cost of multiple launches and in-space assembly. Gossamer technology, however, will allow spacecraft of this type to be launched as a single package.

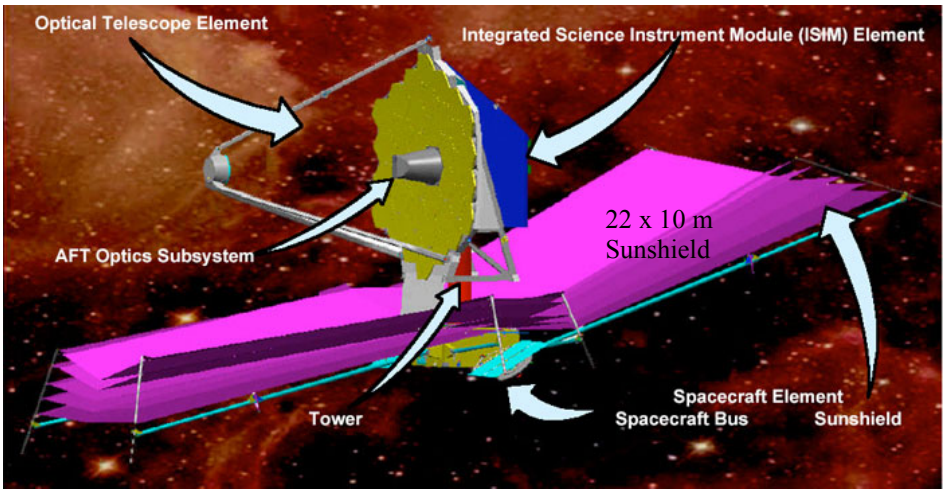

Figure 2 – James Webb Space Telescope

2.2 Solar Sails

Solar sails are among the most studied members of the gossamer family because of the unique propellantless propulsion they provide. Through the momentum transfer of reflected photons of sunlight (sail membranes have highly reflective surfaces) solar sails can generate a small but continuous acceleration on the order of 1.0 mm/s^2. This constant thrust allows travel in non-Keplerian orbits enabling smaller versions less than 100 meters on a side (square sail) to hold an approximately stationary location relative to the Sun or the Earth, such as a polar observing satellite. GEOStorm, a 70 meter square solar sail, will hold position slightly in front of the L1 Lagrange Point, at 0.98 astronomical units (AU) from the Sun and give warning of solar flares. Larger sails, over 150 meters per side, will be able to reach Jupiter in only two years and Pluto in just a decade [3, 6, 17, 19].

A useful level of continuous acceleration is achievable for only a solar sail with very low areal mass densities. The pressure provided by sunlight is just 9.12x10^{-6} N/m^2 at one AU, meaning that the spacecraft must be very large, as discussed above, and very lightweight – less than approximately 20 grams per square meter overall, including payload – to generate acceptable acceleration [7, 20]. Suitable membranes are less than 5 μm thick with areal densities less than 7 g/m^2 [21, 22]. For comparison, standard 8.5 x 11 inch white paper is 100 μm thick with a density of 75 g/m^2. While static and dynamic characterization of structures normally requires the attachment of accelerometers or other measurement sensors, the added mass and stiffness of potentially hundreds of these physically attached devices could drastically alter the properties of the membrane structure being evaluated. Therefore, a totally non-contact measurement method such as photogrammetry is preferred.

3. PHOTOGRAMMETRY AND VIDEOGRAMMETRY

Photogrammetry and videogrammetry were selected as the measurement methods for study and development because of their unique ability to take full-field, non-contact data. Both are mature and complicated metrology methods that will be described here in abridgement.

3.1 Overview

Photogrammetry is defined as the science of making three-dimensional measurements from photographs. The majority of these measurements are generated from aerial photographs and used to create topographic surface maps of large areas or land features. Close-range photogrammetry, the technique detailed below, measures objects several orders of magnitude closer to the camera in much greater detail than aerial topography. It is a complex and mature scientific method that will be only briefly discussed here. For comprehensive coverage, see References 9-13 and 23-25. Specific to the applications discussed here, photogrammetry can be thought of as generating computer models from photographs, as shown in Figure 3. Several aerial photographs, such as the one in Figure 3(a) of a building in Frankfurt, Germany, were used to create the 3-D digital model shown in Figure 3(b) [26].

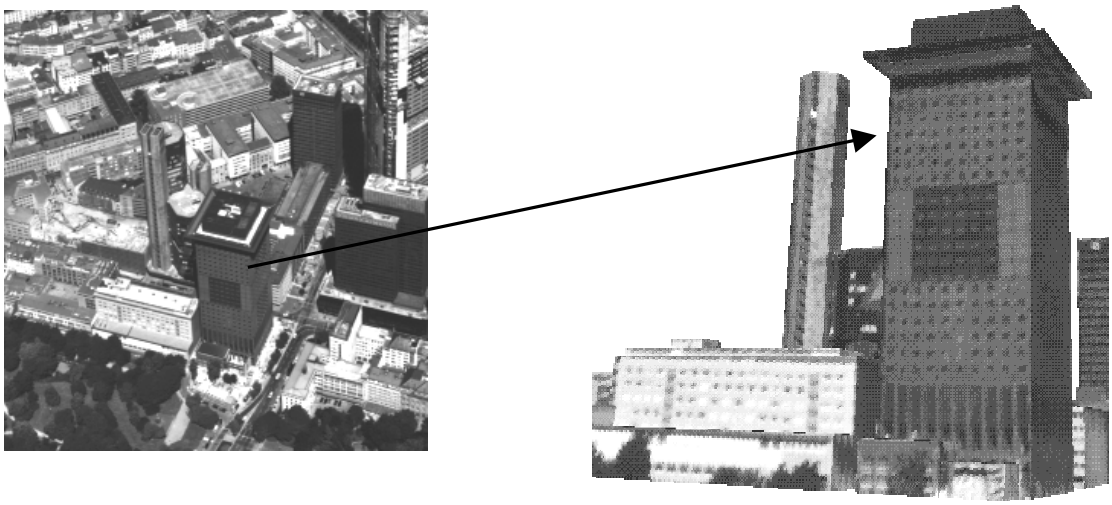

(a) Aerial photograph (b) Computer model

Figure 3 – Aerial photogrammetry example

In Figure 3 only the corners and edges of the building were used to create the model, yielding a low measurement density. The building sides were all assumed to be perfectly flat, and no information concerning possible surface features was obtained (the surface detail in the computer model was mapped from the images, not calculated). Applied to gossamer structures, measuring only the corners and edges of a square solar sail 100 meters on a side will not provide adequate detail about surface features or contours, making accurate static and dynamic characterization impossible. To increase the density of measurement points, a grid of targets is used. The final result of a photogrammetric measurement performed in this manner is a three-dimensional "point cloud" that can serve as a detailed computer model. The models can then be evaluated to generate any desired measurements.

3.2 The Photogrammetric Process

The basic photogrammetric process can be broken up into four steps as follows: camera calibration, high contrast images, target marking and matching, and bundle

adjustment. Each of these steps builds upon the previous to generate high-quality surface measurements.

3.2.1 Camera Calibration

The first step in the photogrammetric process is the calibration of the cameras. This procedure, described in detail in References 9-11 and 25, calculates the focal length (zoom), location of the principal point, radial lens distortion, and decentering lens distortion of each camera. While some of these parameters can be estimated, such as the focal length of the lens and the principal point location, the calibration process measures them to micrometer precisions. For example, the principal point can be estimated to be at the center of the imager; however imperfections in the lens and internal camera components, slight inaccuracies in the manufacturing and assembly processes, etc. cause this assumption to be inaccurate. Knowledge of the lens distortion and the location of the principal point enable the computer to compensate for any deviation of the recorded image from that recorded by an ideal pin-hole camera.

The radial and decentering (tangential) lens distortions are described by Equations 1-3 and 4-5 respectively:

$$\delta r = K_1 r^3 + K_2 r^5 + K_3 r^7 \qquad (1)$$

$$r^2 = (x - x_0)^2 + (y - y_0)^2 \qquad (2)$$

$$\left.\begin{aligned} \delta r_x &= \delta r (x - x_0)/r \\ \delta r_y &= \delta r (y - y_0)/r \end{aligned}\right\} \qquad (3)$$

$$\delta x = P_1[r^2 + 2(x - x_0)^2] + 2P_2(x - x_0)(y - y_0) \qquad (4)$$

$$\delta y = P_2[r^2 + 2(y - y_0)^2] + 2P_1(x - x_0)(y - y_0) \qquad (5)$$

where δr is the radial displacement of an image point, (x,y) are the coordinates of the object point on the imager, (x_0,y_0) are the coordinates of the principal point, K_1, K_2, and K_3 are calculated radial coefficients, and P_1 and P_2 are calculated tangential coefficients [9, 25].

The radial distortion (δr) is caused by variation in angular magnification as a function of angle of incidence. It creates either a "barrel" or a "pin cushion" effect in which images appear to billow toward or away from the center. As rays of light pass through the lens and aperture of the camera, they are distorted slightly by the glass and the fact that the aperture is not actually an infinitesimally small point. As shown in Figure 4, angles i (angle of incidence) and α are equal only for the ideal case corresponding to no refraction through the lens and an infinitesimally small aperture. In reality, however, the rays of light bend when passing through the lens and aperture, meaning that not only are i and α not equal, but the ratio of i to α is not constant over all values of i. This discrepancy is called the radial lens distortion, which is resolved into two components, δr_x and δr_y in Equation 3 above. The maximum radial lens distortions for the cameras used in the applications in Chapters 7 and 8 are as high as 240 microns, corresponding to tens of pixels at the edges of the imager (see Appendix A).

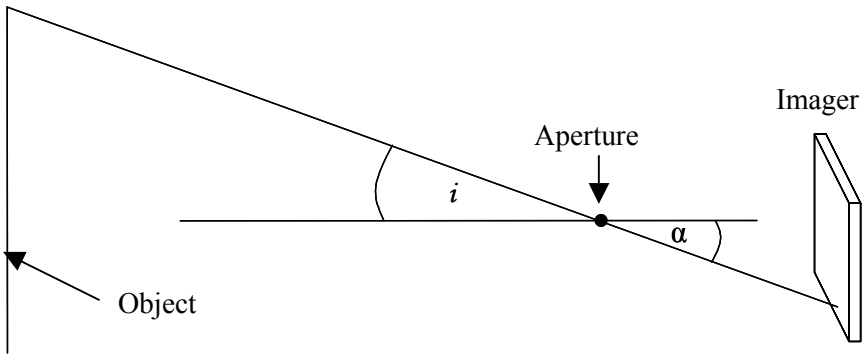

Figure 4 – Radial lens distortion angles

Equations 4 and 5 show the calculation of the decentering, or tangential, lens distortion. This distortion is caused by any misalignment of the lens components, and the coefficients P_1 and P_2 depend on the camera focus setting. In general, as a camera is focused, pieces of glass within the lens move relative to each other. This movement is not exact, however, and the glass pieces tend to be slightly misaligned causing the rotational symmetry of the lens to be imperfect, creating a tangential distortion. Because the lens misalignment, and therefore P_1 and P_2, is unique for every focus setting, a constant focus setting must be maintained after calibrating the camera. To ensure that the focus setting could be repeatedly set to the same value, every camera discussed below was calibrated and used exclusively at infinity focus [9, 25].

Using focal length, principal point location, radial lens distortion, and decentering lens distortion values calculated in the camera calibration process, the photogrammetric software automatically removes any distortions of the images due to those parameters, enabling accurate measurements. To correct for possible changes in the calibrations over time and maintain measurement accuracy, the cameras were re-calibrated periodically. The parameters obtained from multiple calibrations are listed in Appendix A.

3.2.2 High Contrast Images

Figures 5 and 6 show the second step in the photogrammetric process, the taking of high-contrast images. Traditionally, high contrast for measurement purposes is obtained using attached retro-reflective targets, shown in Figure 5, and underexposed images, shown in Figure 6. The camera flash illuminates the targets, which reflect light back to the camera hundreds of times brighter than a diffuse white surface. The underexposure darkens the rest of the image to the point where only the bright targets are

clearly visible, creating a binary white-on-black image as shown in Figure 6. The binary nature of the images permits automatic and accurate detection of the target locations. While retro-reflective targets are highly effective and considered the industry standard, the added thickness, mass, and stiffness, combined with the required attachment time for potentially thousands of targets necessitate an alternative non-contact method for use on solar sails. The development and application of an approach using projected dots of light as targets is discussed in Chapters 6 through 8.

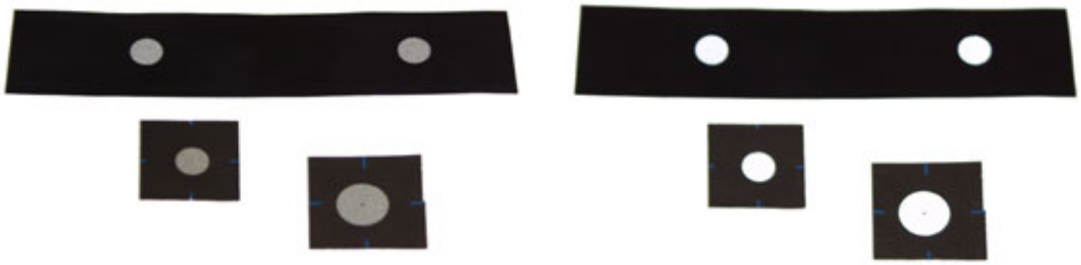

(a) With camera flash off (b) With camera flash on

Figure 5 – Retro-reflective targets

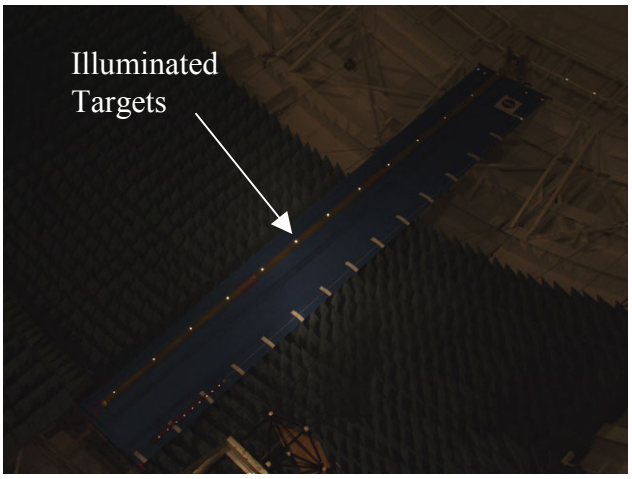

Figure 6 – Underexposed image of a 7 m boom used in photogrammetric measurement

3.2.3 Target Marking and Matching and the Bundle Adjustment

In the third step of the photogrammetric process, multiple binary (high-contrast) images are loaded into the photogrammetric software and associated with the appropriate lens and camera calibration parameters. The targets are marked to sub-pixel accuracy using a centroiding process based on a least squares matching (LSM) algorithm with an elliptical template to account for off-normal viewing angles (see References 11 and 23), and the resulting points corresponding to the exact centers of the targets are matched across the photographs, as shown in Figure 7. An algorithm called a bundle adjustment is then run (step four) which simultaneously iterates on the camera locations and orientations from which the photographs were taken – a process called resection – and also calculates the 3-D point locations and corresponding precision values – a process called intersection. To obtain these point locations in three-dimensional space, a line is projected from each camera to the point, also shown in Figure 7. Note that projected light rays are infinitesimally wide, so in general the rays from multiple cameras never intersect. However, they do establish the bounds of an intersection region. The intersection region in space is assumed to contain the true point location. This method of calculating point locations requires each target to appear and be marked in at least two images. Note that using more photographs in the photogrammetric process increases the redundancy and hence the accuracy.

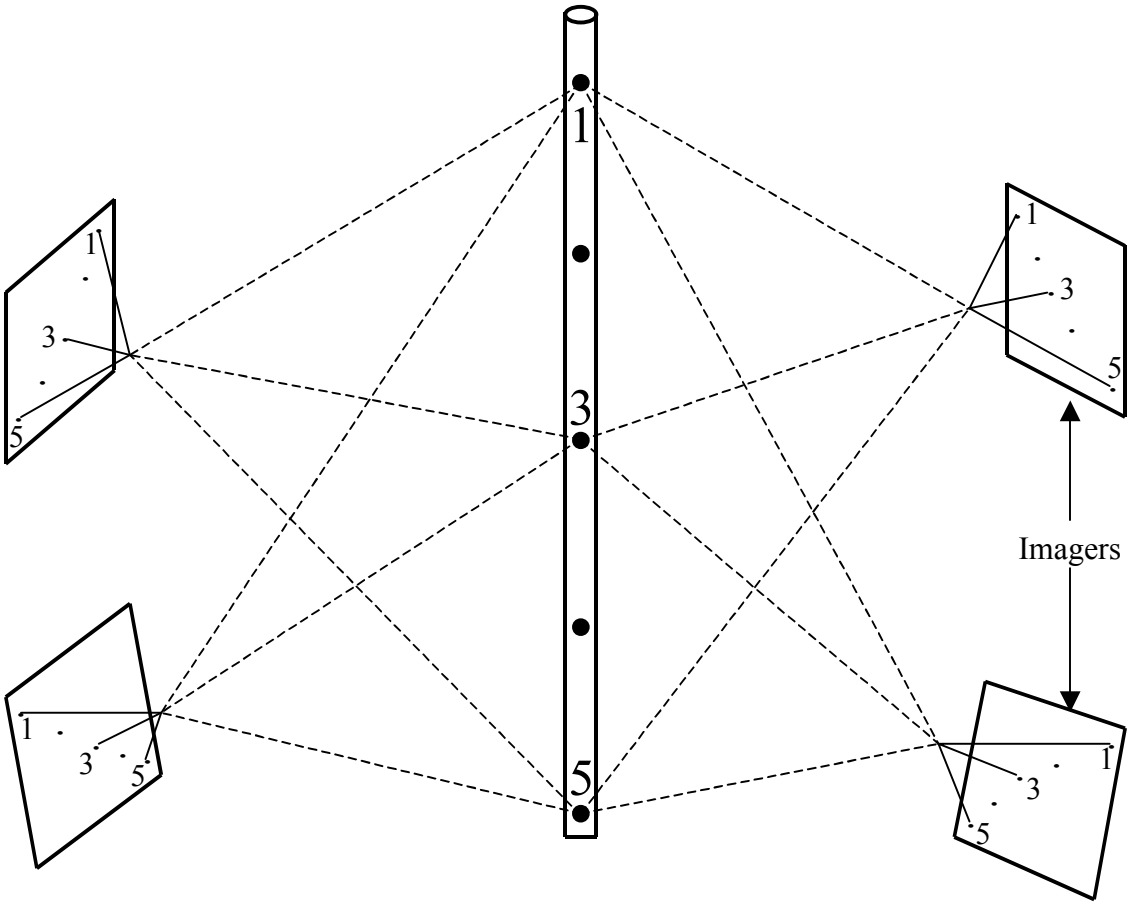

Figure 7 – Matching and triangulation of points

3.2.4 Point Cloud

The final result of the photogrammetric process is a set of 3-D points called a point cloud that, with an axis and scale defined, can be exported and measured. Figure 8 shows a simple example in which photogrammetry was used to measure the straightness of the seven meter inflatable boom in Figure 6. The curved line shows the measured locations of the targets on the boom and is compared with a best-fit straight line. Note that the graph shown in Figure 8 is intended only to demonstrate one of many types of possible measurements from photogrammetric data and is not meant to provide any specific results.

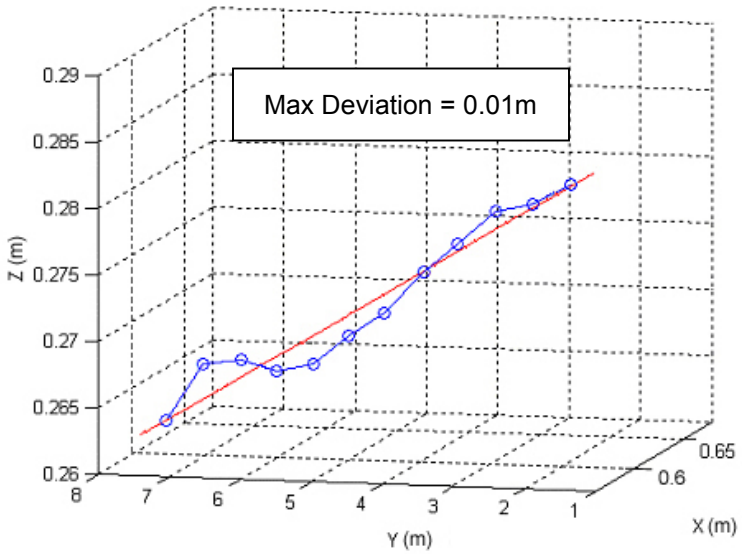

Figure 8 – Exported point cloud and best-fit straight line

3.3 Videogrammetry

Videogrammetry expands the methods and techniques of photogrammetry to multiple time steps creating dynamic data. The first images from multiple synchronized sequences of images are processed as a stand-alone photogrammetry project. The points are then tracked through the sequences of images with the camera locations assumed to be stationary, and at each time step the intersection is performed creating individual sets of three-dimensional points. The sets of points can then be linked together, tracking the movement of the point cloud from the first time step throughout the entire image sequence. This dynamic data can then be animated and analyzed. For a more detailed discussion of videogrammetry, see References 13 and 24.

4. HARDWARE

The hardware required for photogrammetric and videogrammetric measurements are separated into two categories: cameras and projectors. All of the cameras and projectors used to make measurements are described in detail, as well as the advantages and disadvantages of using each.

4.1 Still Cameras

Photogrammetry, as discussed previously, uses photographs to make static shape measurements. While large format film cameras can be more accurate than digital cameras because of their greater resolution, digital images are preferred for the applications discussed in the following chapters due to the ease of import of measurement data and analysis with computers. Several different digital still cameras are available to consumers and professionals. The applications discussed below will demonstrate a progression from consumer grade hardware and software to test the feasibility of the method for solar sail applications to professional and custom equipment to refine the process and generate high quality measurements. The applications in Sections 7.1 and 7.2 used four consumer grade Olympus E20n cameras (Figure 9(a)) while the application in Section 7.3 used four professional Kodak DCS 760M cameras (Figure 9(b)). These chapters also discuss the pros and cons of the transition from the consumer cameras to the professional. Figure 9 shows the cameras with attached ring flashes, which provide more uniform illumination of targets than standard built-in flashes. Specifications for both cameras are listed in Table 1 below.

(a) Olympus E20n with ring flash

(b) Kodak DCS 760M with ring flash

Figure 9 – Digital still cameras

Table 1 – Still camera specifications

	Olympus E20n	Kodak DCS 760M
CCD size (pixels)	2560 x 1920	3032 x 2008
CCD size (mm)	8.704 x 6.582	27.288 x 18.072
Dynamic Range	8 bit color	12 bit monochrome
Lenses		
Type	Non-removable	Removable
Focal Length (mm)	9 – 36	Variable (25.0)
Aperture	f/2.0 – f/11.0	Variable (f/2.8 – f/22)

The professional-grade Kodak camera has obvious improvements over the consumer-grade Olympus camera, as indicated by the data shown in Table 1. It has a six megapixel imager versus the five megapixel Olympus. The charge coupled device (CCD) imager in the Kodak is physically larger than the Olympus increasing its light sensitivity, and the Kodak has a greater dynamic range. The Olympus is manufactured with an attached zoom (variable focal length) lens while the lens of the Kodak is removable meaning the camera can be fitted with a variety of fixed focal length and zoom lenses. Parenthetical values in Table 1 denote the values for the lens used in the applications. The aperture size is variable on both cameras to allow the user to change the amount of light striking the imager. Larger apertures, while enabling shorter exposure times used to eliminate blurring when taking photographs with a hand-held

camera, result in a shorter depth of field than smaller apertures. Accordingly, small apertures (f/9.0 – f/11.0) were used in both cameras to ensure that objects both close to and far from the cameras would be simultaneously in focus. The differences in the two cameras with respect to the accuracy and precision of the measurements they provide are discussed in detail in Chapter 5. While the results obtained using the professional camera are considerably better than those obtained using the consumer camera, the improvement comes at a price. The Kodak DCS 760M is approximately six times the cost of the Olympus E20n.

It should also be noted that digital cameras are capable of performing many operations that enhance the produced images. Color balancing, image compression, anti-aliasing filters, sharpening, etc. all make the image look better, but complicate scientific measurements by altering or adding interpolation. To minimize the negative impact of the enhancements, all filters and sharpening were turned off and the images were stored with the least amount of compression possible.

4.2 Video Camera

Videogrammetry, like photogrammetry, relies on multiple images from various viewing angles to generate the desired 3-D models. To yield a sequence of images in time, the method requires multiple images at each time step, necessitating two or more synchronized video cameras. The Pulnix TM-1020-15 digital video camera (Figure 10) is a high quality scientific video camera, and a two-camera synchronized Pulnix system was used for the videogrammetry test. Figure 10 shows the camera with an attached fiber optic ring light used to provide even illumination of the retro-reflective targets. The

specifications for this camera are listed in Table 2 below. As noted previously, parenthetical values indicate the parameters of the specific lens used in the test.

Figure 10 – Pulnix TM-1020-15 digital video camera with ring light

Table 2 – Video camera specifications

	Pulnix TM-1020-15
CCD size (pixels)	1008 x 1018
CCD size (mm)	9.072 x 9.162
Frame Rate (Hz)	Variable, 15 max
Dynamic Range	10 bit monochrome
Lens	
Type	Removable
Focal Length (mm)	Variable (12.5)
Aperture	Variable (f/1.4 – f/22.0)

The TM-1020-15 has a one megapixel resolution, lower than either of the still cameras discussed in Section 4.1, but does have a large 9 μm pixel size like the Kodak DCS 760M. This resolution is typical, however, of scientific-grade video cameras operating at maximum frame rates of 15 Hz. At one megabyte per image, fifteen images per second, and two cameras, the system computer must store 30 MB of data each second at maximum frame rates. During data collection the image sequences are stored in the computer's RAM and are only copied to the disk after the test. The video cameras have

dynamic ranges and lens properties that are similar to those of the still cameras. All of the cameras discussed above enable non-contact, full-field, simultaneous data collection.

4.3 Projectors

As discussed previously, traditional photogrammetry uses attached retro-reflective targets that would add unacceptable mass and stiffness to the ultra-thin membranes being measured. To avoid these unwanted effects, grids of circular targets were projected onto the test articles by the projectors shown in Figure 11. Figure 11(a) shows the Kodak Ektagraphic, a consumer-grade 35 mm slide projector that uses a fairly low-power incandescent bulb.

The modest intensity of the Ektagraphic combined with the high reflectivity of the aluminized solar sail membranes necessitated exposure times as long as 30 seconds to obtain images of optimal contrast. To combat these long exposure times, a theater version of the Kodak Ektagraphic (Figure 11(b)) was subsequently used. It uses a high-power halogen bulb thereby producing higher intensity patterns than the consumer version. The greater intensity allows the exposure times of the cameras to be decreased significantly. To upgrade another step to professional hardware, a Geodetic Systems Inc. (GSI) Pro-Spot projector (Figure 11(c)) was used in the application discussed in Section 7.3. It is a high-intensity flash projector capable of projecting up to 22,500 dots versus the maximum of 5,500 dots for the other projectors. The Pro-Spot is part of GSI's turn-key industrial photogrammetry system, but was purchased separately for use in measuring solar sail test articles.

(a) Kodak Ektagraphic

(b) Kodak Ektagraphic Theater

(c) Geodetic Systems Inc. Pro-Spot

(d) Proxima LX2 Digital

Figure 11 – Projectors

The Proxima LX2 digital projector (Figure 11(d)) was used for the videogrammetry application. Again a consumer product, its low intensity and resolution would limit its usefulness in measurements of highly reflective membranes. The projector did not, however, negatively affect the accuracy or precision of the videogrammetric measurement here because the test article in the experiment is comprised of diffuse white (non-aluminized) Vellum membranes. The major advantage of the digital projector is its ability to project custom dot patterns from computer files that can be easily and rapidly altered.

5. ACCURACY, PRECISION, AND REPEATABILITY

Accuracy, precision, and repeatability quantify the error and noise present in a measurement. The photogrammetric measurements discussed here have three sources of experimental error and noise: the cameras, the projector, and the imaged targets (measured object). Any, or more likely all of these components or bodies may move slightly during data collection or in some other manner introduce noise and error that detract from the overall quality of the measurement. The error caused by the cameras and targets are tracked or estimated by the photogrammetry software, and are examined in detail below. The error caused by the third body in the system, the projector, is not, however, accounted for individually as in the case of the other two bodies. Rather, the projector is assumed to be stationary, and the error and noise for which it is responsible is grouped with the other two error sources.

5.1 Overview

The quality of any measurement can be described by three separate terms, accuracy, precision, and repeatability. The accuracy of a measurement expresses how close the process came to producing the true value. It can only be determined by comparing the results obtained using one measurement method to the results obtained from a higher quality system known to be at least twice as accurate. In the case of the measurements discussed here, higher quality comparable systems were not available for the static cases; however the level of maturity of photogrammetry as a scientific process, the error estimates produced by the software, and qualitative assessment are considered sufficient validations of the measurements. In the dynamic case, the videogrammetric results were compared with those of a high-end laser vibrometry system.

The precision of a process can be thought of as the resolution of the measurement. For example, the measured weight of a cruise ship is usually precise to about one ton whereas the measured weight of a human being is usually precise to about one pound. The precision of the photogrammetric measurements performed below is discussed in the next section. Finally, the repeatability of the system is the ability of a process to generate the same results while measuring the same object multiple times. These three factors are all relevant to a discussion of the overall quality of a scientific measurement. [23, 25]

5.2 Photogrammetric Error Estimates

The commercial photogrammetry software used in the applications below reports three error estimates: marking residual, tightness, and precision [23]. These estimates are calculated either directly at the end of the photogrammetric process or by error propagation techniques. A finite amount of error is present in all of the initial steps of the photogrammetric process, from the camera calibration to the capturing of the images to the marking of targets. These errors are embedded within the inputs of the bundle adjustment algorithm and are therefore propagated through the calculation. The software tracks or estimates the errors inputted into the algorithm, and produces precision information after the processing is complete. The marking residuals and tightness information are calculated independently at the end of the process and are described below.

Photogrammetric precisions are usually expressed as ratios of the form 1:10,000, meaning one part in 10,000. In this case, if the measured object is one meter in size, the measurement would be precise to one meter divided by 10,000, or 0.1 millimeters (100 microns). The manner in which this error information is presented varies depending on

the software package, but for all of the applications discussed here there is a 95% probability (plus or minus two standard deviations) that the true location of the point falls within the error ellipsoid created from the precision numbers for the X, Y, and Z directions. X, Y, and Z precisions for each three dimensional point are calculated by the error propagation technique discussed previously. Tightness estimates are calculated by determining how close the projected rays come to intersecting the point (see Section 3.2), and residuals are calculated for each point on each image by determining how far the point in the image is from the point projected from the calculated 3-D location. Precision estimates are reported in working units of the project, tightness estimates in percentages, and marking residuals in pixels [23].

5.3 Camera-Related Factors

Physical properties of the cameras used the photogrammetric process have a significant impact on the precision and accuracy of the measurement. The type of imager, type of lens, quality of manufacture, etc. are important contributing factors. Several properties of the Olympus cameras detract from maximum achievable accuracy when compared with the Kodak cameras. While both Olympus E20n and Kodak DCS 760M cameras use CCD imagers, the E20n has a five megapixel resolution compared to the six megapixel DCS 760M (Table 1). The higher resolution of the professional camera yields a greater number of pixels per target and therefore increases the amount of information being used in the LSM centroiding phase, making the process more accurate at finding the exact center of the targets. The physical size of the pixels on the Kodak imager is 9.0 microns versus the smaller 3.4 microns of the Olympus. Larger pixels have a greater sensitivity to light and reduce the amount of noise present in images, and are

therefore nominally twice as precise [25]. In summary, the Kodak DCS 760M has a greater number of more sensitive pixels than the Olympus E20n, which makes it more precise in scientific measurements.

The third row of Table 1 shows the difference in the dynamic range of the two cameras. The consumer Olympus is an eight-bit color camera that produces standard eight-bit images while the professional Kodak is a monochrome twelve-bit camera. The increase in the dynamic range of the professional over the consumer camera again yields a greater sensitivity to light and therefore accuracy. Another limiting factor of the Olympus camera is its color CCD. To produce color images, most cameras attempt to mimic the structure of the human eye. The cones of the eye, which sense color, are comprised of three separate types. Approximately 60 percent of the cones see only green, 30 percent see only red, and 10 percent see only blue. The brain then combines the intensity information from each of these sets to create a single, cohesive color image. Like the cones of the human eye, each pixel on a digital imager can only see one color. Most CCD's are comprised of 50 percent green pixels, 25 percent red pixels, and 25 percent blue pixels arranged in what is called a Bayer checkerboard pattern, roughly paralleling the distribution of cones in the eye. For each image, the on-board camera processor runs an interpolation algorithm to assign each pixel intensity values for the other two colors it cannot see, thereby creating a cohesive image. The interpolation reduces the effective resolution of color compared to monochrome cameras for photogrammetric measurements [27].

Information regarding the lenses of the two cameras is also listed in Table 1. The built-in zoom lens on the Olympus has several more glass pieces through which light must pass to reach the imager, leading to greater distortion of the light rays and again

decreasing its accuracy. The fixed focal length lenses used on the Kodak cameras are inherently more stable for precision photogrammetric measurements than zoom lenses.

From the above discussion one might receive the impression that the consumer Olympus cameras are drastically less accurate than the professional Kodak cameras, which is not the case. The Olympus E20n is a high-quality single lens reflex (SLR) consumer camera (fixed lens) that has produced measurement precisions up to 1:30,000, or one-fourth that of top-end industrial turn-key systems at less than one fiftieth of the cost [28]. The Kodak DCS 760M camera is approximately five times the cost of the Olympus camera, yet only doubles or triples its measurement precision. In effect, it is easy to get an answer with photogrammetry using basic hardware, but as with any measurement system, a principle of diminishing returns applies making it expensive to obtain the highest measurement precision and accuracy.

As stated previously, videogrammetric measurements were performed using only two Pulnix TM-1020-15 video cameras instead of the four cameras used in the static measurements. More cameras with greater resolution and higher frame rates can be added to the system, but with each improvement comes a requirement for higher computer bandwidth and a larger total amount of data that must be stored by the computer per unit time. To maximize the accuracy with only two cameras, however, the TM-1020-15 does use large 9.0 micron pixels and a monochrome CCD. Noise level tests for the Olympus, Kodak, and Pulnix systems were conducted and are discussed in the following section, and the precision of the individual measurements are discussed in the sections detailing the four application examples.

5.4 Noise Tests

Knowledge of the signal-to-noise ratio of experimental data is important to understanding the results of a test. It is essential that results are obtained from actual response of the system and not from background noise inherent in every experiment. Related to photogrammetry, the noise level of the camera systems is one of the factors governing measurement resolution, meaning features cannot be characterized with confidence below the noise floor. For dynamic data the noise floor determines the smallest displacements from one frame to the next that can be detected.

The noise floor of each of the camera systems was measured by tracking the calculated position of stationary points over a period of time. The still camera systems took time-lapse images over several minutes while the video cameras simply recorded stationary points as part of a dynamic measurement. The test setup is shown in Figure 12 below.

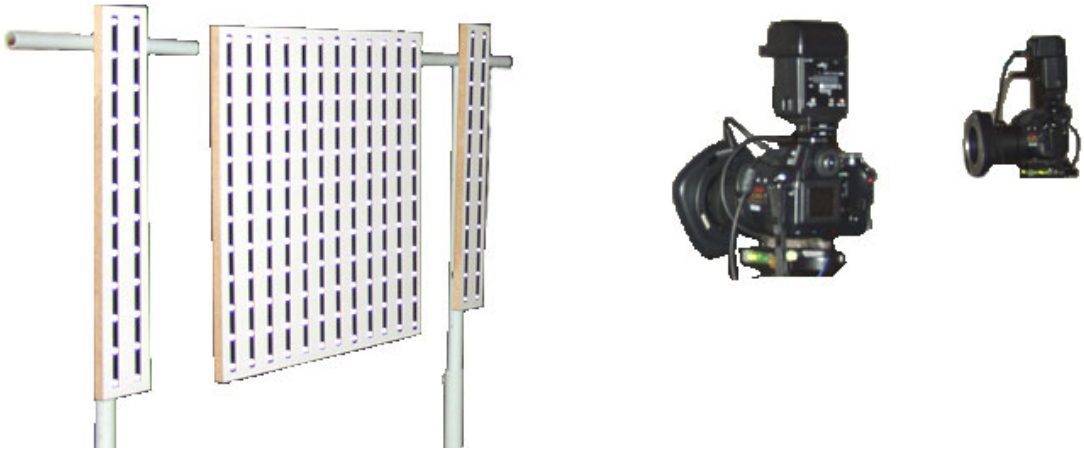

Figure 12 – Noise test setup

Three boards with attached retro-reflective targets on strips of black tape were imaged. Because attached instead of projected targets were used, the third source or body of error (projector) was eliminated allowing direct calculation of the noise from only the

cameras and targets. The slender boards on the left and right were mounted on stationary stands while the square board in the middle was allowed to swing freely to establish a baseline against which to compare the stationary points (see Reference 24). For all three cases (one for each camera type), the computed locations of the points on the stationary sidepieces were plotted versus frame number, called epochs, to generate the desired noise measurements and are shown in Figures 13, 14, and 15. Also shown in these figures is the difference between the maximum and minimum points in the series, denoted by the Δ value. Note that in Figures 13 and 14 one epoch is equal to 12 seconds and in Figure 15 each epoch is equal to one fifth of a second.

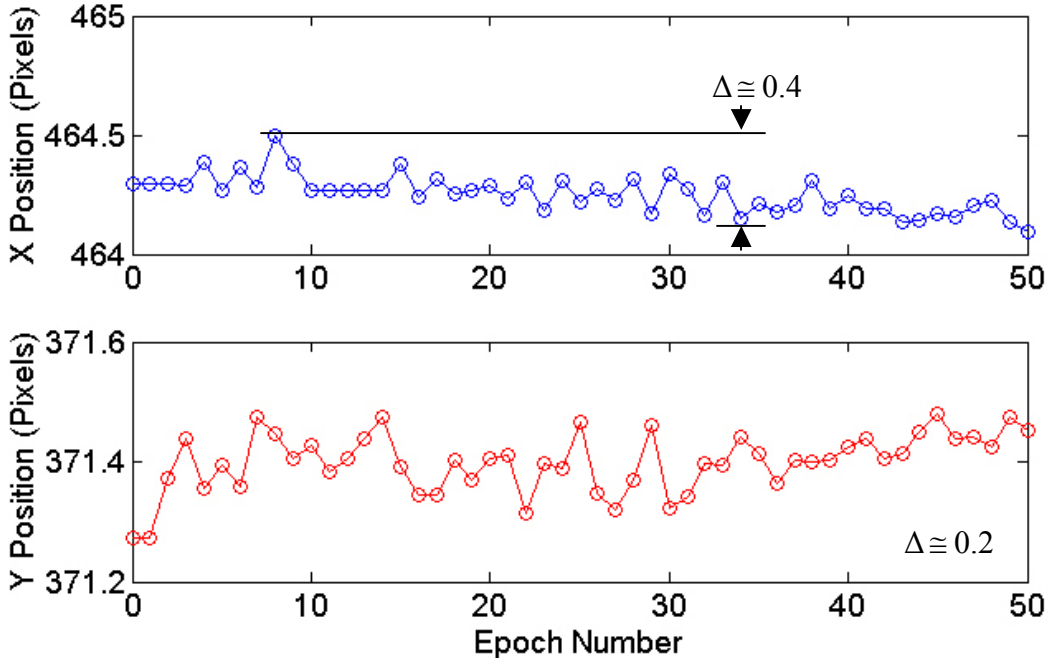

(a) Left camera

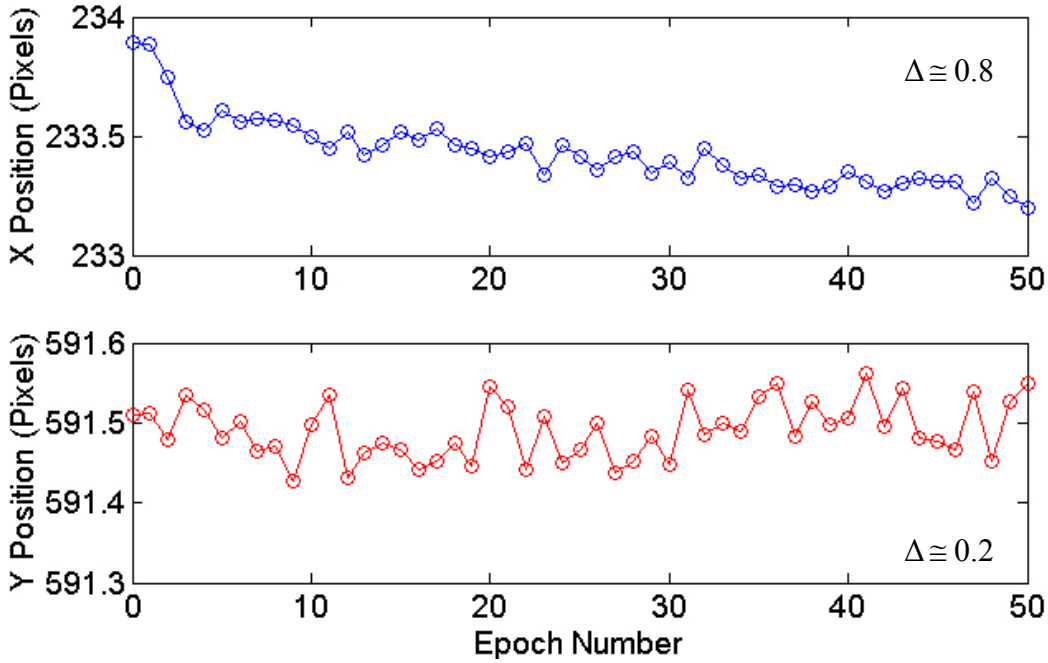

(b) Right camera

Figure 13 – Olympus E20n plots of a stationary point over time

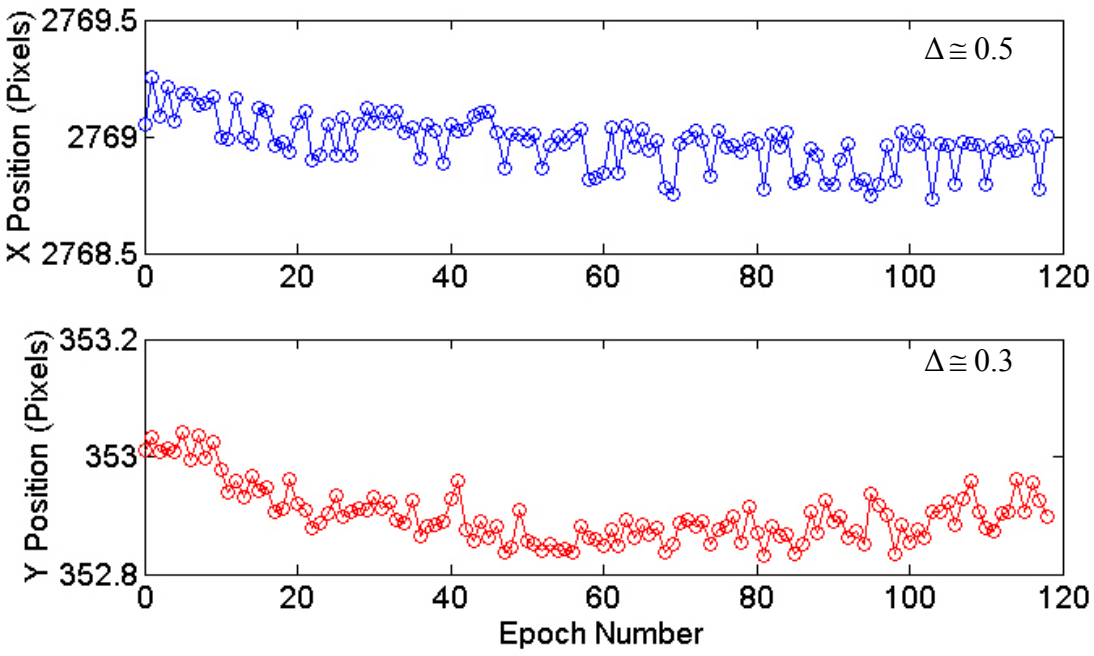

(a) Left camera

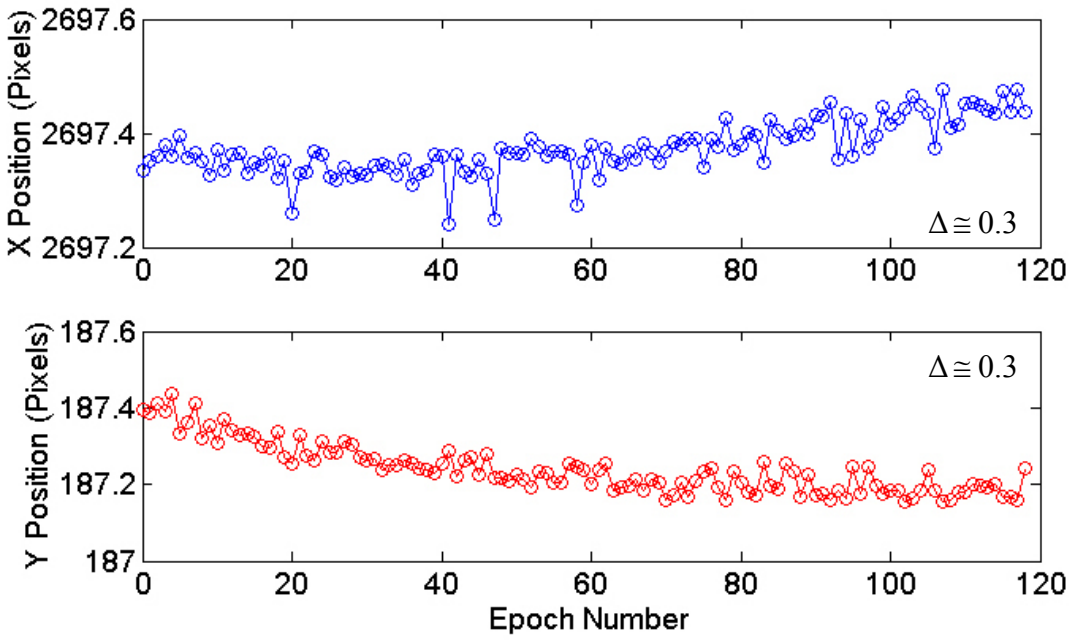

(b) Right camera

Figure 14 – Kodak DCS 760M plots of a stationary point over time

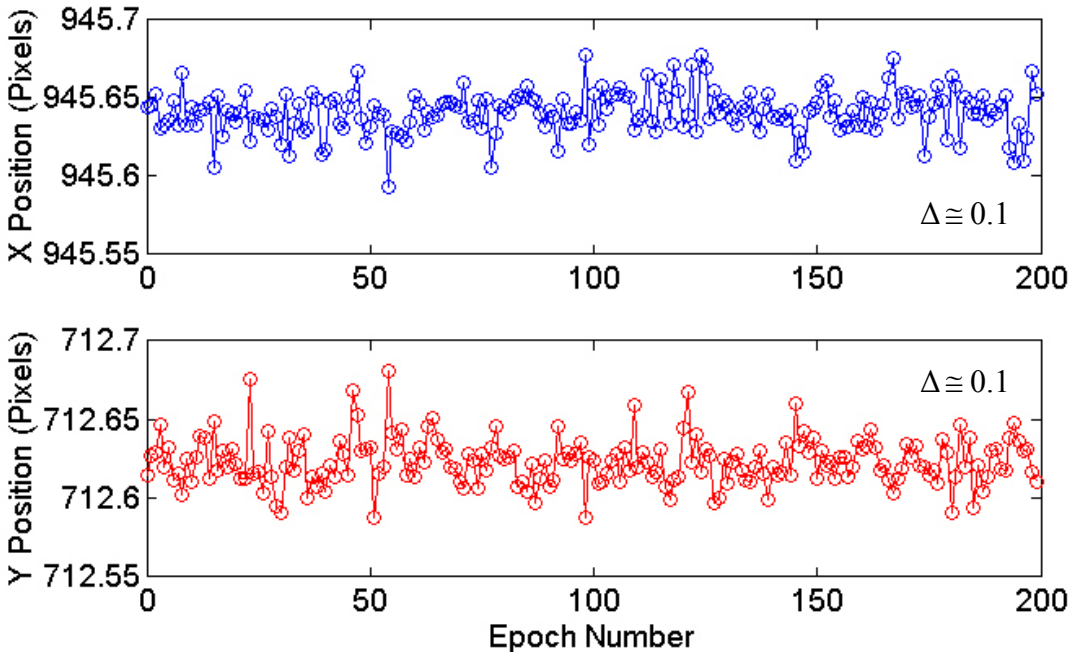

(a) Left camera

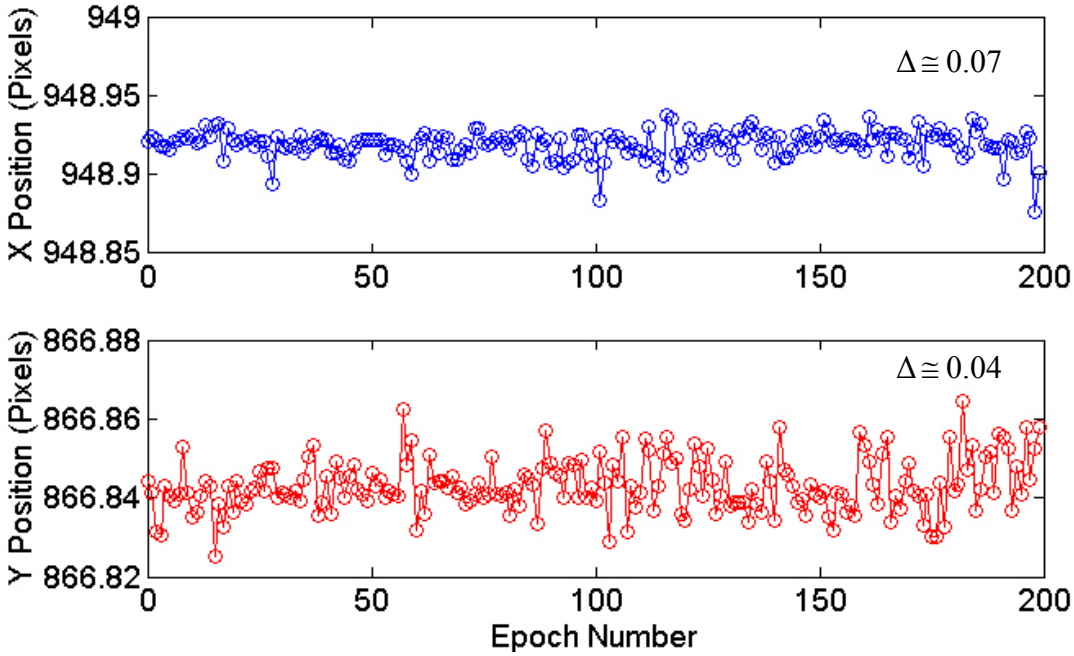

(b) Right camera

Figure 15 – Pulnix TM-1020-15 plots of a stationary point over time

Table 3 – Standard deviations of noise plots

	Olympus		Kodak		Pulnix	
	Left	Right	Left	Right	Left	Right
X Position Mean (pixels)	464.252	233.428	2786.975	2697.373	945.641	948.920
Y Position Mean (pixels)	371.400	591.491	352.901	187.241	712.623	866.843
σ_x (pixels)	0.077	0.15	0.11	0.046	0.014	0.0086
σ_y (pixels)	0.050	0.036	0.049	0.065	0.015	0.0067
2 σ (pixels)	0.125	0.185	0.155	0.110	0.030	0.015
Overall Noise (pixels)	0.185		0.155		0.030	

The plots in Figures 13 through 15 show the calculated center of a stationary point using the Olympus, Kodak, and Pulnix camera systems. Ideally these graphs would exhibit no trends or bias, and simply show a random scatter plot, as would be expected from noise. Bias is evident, however, in Figures 13 and 14 and will be discussed below. Table 3 shows the means and standard deviations (σ) of the plots in Figures 13, 14 and 15, without correction for the trends. The row labeled "2 σ (pixels)" indicates that 95% (2*σ where σ is the average of σ_x and σ_y) of the noise in the left camera of the Olympus system falls within 0.125 pixels of the mean value and within 0.185 pixels of the mean value in the right camera. The larger of the two values, 0.185 pixels, is considered the overall noise floor of the Olympus system. Similarly, the overall noise floors of the Kodak and Pulnix systems are calculated to be 0.155 and 0.030 pixels respectively.

Expressed as a ratio of noise to number of pixels in the x-direction on the imager, the Olympus E20n noise floor is 1:14,000, the Kodak DCS 760M noise floor is 1:20,000, and the Pulnix TM-1020-15 noise floor is 1:34,000. Note that with the trends removed, the noise estimates for the Olympus and Kodak systems can be reduced by at least a factor of two. The targets imaged in photogrammetric measurements usually appear at least five pixels in diameter, and are therefore well above the level of disturbance caused

by noise present in the systems. The motion of the object recorded from one image to the next in the videogrammetry test was also well above the noise floor of the system.

The plots in Figures 13 and 14 above show unexpected trends in the movement of a photographed stationary point. Obviously the calculated position of a stationary point should not move in any predictable manner over time, meaning the apparent motion is caused by random noise present in the system. This noise might include air currents, ground vibrations, settling of the tripod or board stand, electronic static, camera heating etc. The Olympus and Kodak camera systems were tested until the trend appeared to level, leading to the disparity in number of epochs used.

To examine the effects of the biases present in the noise data from each camera system, the total spread of the series was printed on the plots in Figures 13 – 15. The spread, Δ, is equal to the difference in the maximum point value in the series and the minimum point value in the series. Figure 13 shows that the Olympus cameras have the largest Δ's, caused by the most pronounced trends in the data. The Pulnix cameras (Figure 15) have the smallest Δ's, as little or no bias affects the system. A larger Δ value indicates more uncertainty in the location of the photographed points and a greater probability of noise influencing the measurements.

To visualize the biases, occurrence densities are plotted in Figure 16 for each camera system. The graphs were generated by dividing the Δ value for each series into 14 equal blocks and summing the occurrence of points within each block. Density plots for the most biased of the four series from each of Figures 13, 14, and 15 are shown. Figure 16(c) shows an approximately symmetric bell curve versus those in Figures 16(a) and 16(b) in the Pulnix TM-1020-15 series, expected from random noise with little or no bias. Most of the points are clustered near the average value of the series, with a minimal

number of extreme points lying outside the curve. Figures 16(a) and 16(b) by contrast show asymmetric curves of the Olympus E20n and Kodak DCS 760M data heavily influenced by a disproportionate number of points at extreme values of the series. These curves clearly demonstrate that the biases present in the Kodak and Olympus camera systems affect the stationarity and therefore randomness of the data, and lead to the conclusion that external, non-random factors influenced the systems.

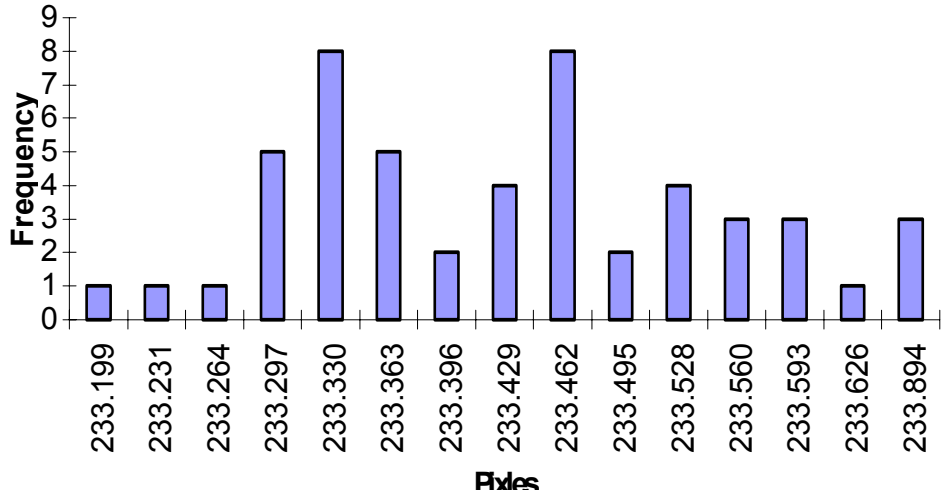

(a) Right Olympus E20N camera measured X position

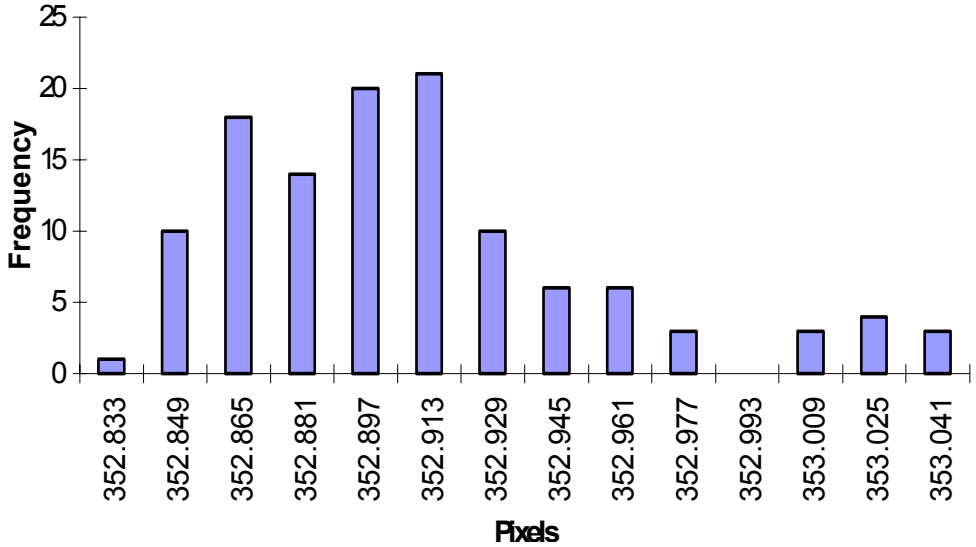

(b) Left Kodak 760M camera measured Y position

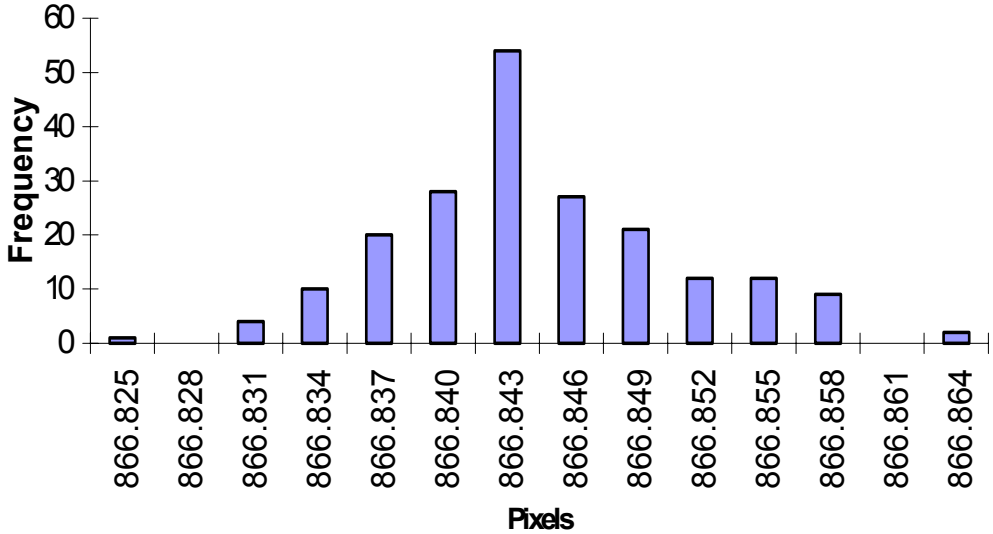

(c) Right Pulnix TM-1020-15 camera measured Y position

Figure 16 – Occurrence density plots demonstrating biases

The biases in the data cause the calculated centers of stationary targets to migrate over time. All of the point centroids in each of the images migrate in a diagonal fashion as shown in Figure 17, a trend that has been observed in other tests. The exact cause of this migration is still under investigation, but is likely due to global effects such as camera heating or tripod settling. Again it should be noted that the size of the measured targets (signal) is much larger than any biases or noise present in the systems.

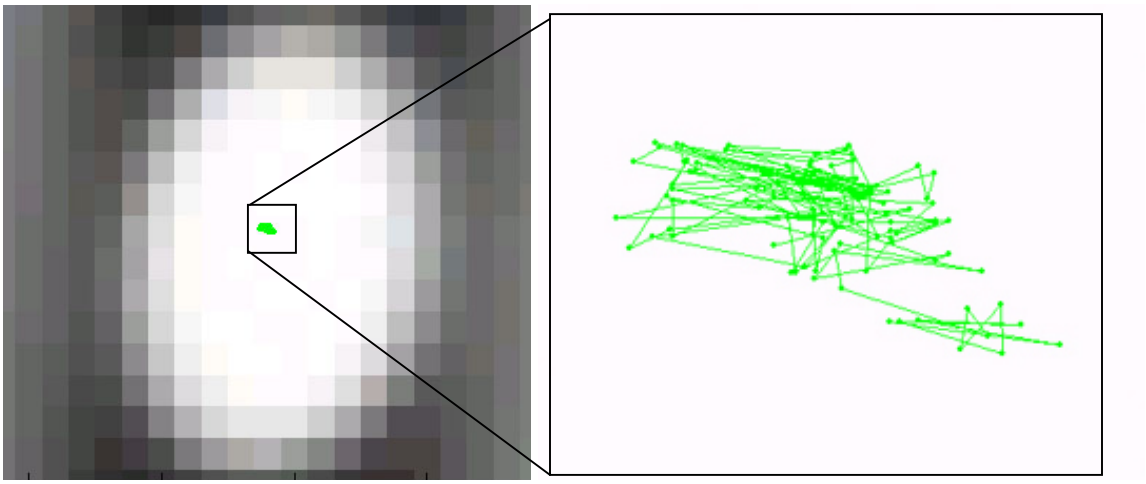

Figure 17 – Migration of a measurement of a target centriod in time

6. RETRO-REFLECTIVE VS PROJECTED TARGETS

High resolution photogrammetric measurements rely on high-contrast images and a high density of targets. For example, the general shape of the boards in Figure 12 could have been measured using only the four corners and four edges, but this does not provide information about the object's surface shape. Attaching retro-reflective targets to the face of the board enables measurement of its contour and surface features, in addition to the edge and corner locations. Projected targets can be used instead of retro-reflective targets to avoid altering the responses of the measured objects, but introduce experimental and numerical complications discussed here.

6.1 Retro-reflective Targets

Retro-reflective targets are manufactured in a variety of shapes and sizes. Circular targets can be punched from sheets of retro-reflective material, peeled off sheets of individual targets, or cut from rolls of tape with targets spaced at a precise, repeating interval. Specific shapes or patterns of targets can be identified as individual codes by photogrammetry software, and pieces of carbonite can be machined to sub-micrometer precision with targets at exact spacing. Retro-reflective targets have been used to measure objects ranging in size from the 305-meter Arecibo Observatory [29, 30], to a five meter inflatable lenticular reflector [10], to micro air vehicles less than 20 centimeters in size. This method of targeting is considered the industry standard in photogrammetric measurements [31].

Retro-reflective targets used in conjunction with flash illumination, fast shutter speeds, and small apertures appear as bright white circles on a black, underexposed background (see Figures 5 and 6). Retro-reflective material is manufactured by bonding

small, silver-coated glass spheres to a substrate, usually a paper-based material. The spheres are approximately 50 microns in diameter and they are attached using about 25 microns of epoxy. The coating on the top halves of the spheres is then chemically removed, leaving only the side by side reflective hemispheres, resulting in a range of intense reflections approximately $\pm 60^{o}$ from normal.

For the majority of close-range photogrammetric applications, the thickness, weight, and attachment time associated with using retro-reflective targets are inconsequential compared to the superior results they provide. When used in gossamer applications, however, the added mass and stiffness may seriously alter the static and dynamic properties being measured. The average thickness of a retro-reflective target is 100 microns including the substrate, significantly greater than solar sail membranes, which can be less than five microns thick. Aside from the additional thickness, the mass and stiffness associated with adding retro-reflective targets to a membrane can have a great impact on its static and dynamic properties. Consider a square solar sail membrane 100 meters on a side. At 10,000 square meters in size, this membrane has a mass of just 70 kg based on a seven gram per square meter areal density. Assuming a modest measurement density of 10 targets per square meter – some applications use 2500 targets per square meter – 100,000 retro-reflective targets would have to be attached to the surface of the sail. The combined mass of these targets may be as much as that of the sail itself. Such a large number of targets would also require an impractical amount of time to attach.

In addition to the physical drawbacks discussed above, a small geometric distortion occurs when using retro-reflective targets. Light from the camera flash reflects off the targets, not the object to which they are attached, meaning that in reality the target

and not the object surface is being measured. The center of the target may be anywhere from 50 to 75 microns from the surface of the object, and adds uncertainty to the measurement, especially when imaging ultra-thin, wrinkled membranes.

6.2 Projected Targets

As an alternative to physically attaching retro-reflective targets, white circular targets were projected onto the solar sail test articles. Called dot projection, this targeting method has several advantages over attached targets. Projected targets do not add mass or stiffness to the object, they do not have to be individually attached, and because the light reflects off the surface of the object, it is the actual surface that is measured instead of the optical center of a target located slightly above the surface. Target patterns, sizes, and densities can also be varied with ease, and there is no risk of membrane damage associated with changing the pattern.

The major drawback of dot projection when used on reflective surfaces such as solar sails involves the non-uniform contrast of the projected patterns. Within the $\pm 60^{o}$ range of retro-reflective targets, almost identical amounts of light will be reflected by all of the targets (a result of the geometry of the spheres of which the material is comprised) regardless of angle to the camera or the reflective properties of the material being measured. The dot projection technique, however, requires a single stationary projector with multiple cameras imaging the created pattern, meaning only this single source of light is used instead of multiple flashes. For materials that scatter light in all directions more or less equally such as diffuse white surfaces like projector screens, the relationship of the camera location to the light source location is inconsequential. The same level of contrast is expected from virtually all camera positions. If the material being measured is

not diffuse but, for example, specular as in the case of the solar sails, each incident light ray is reflected almost entirely in one direction according to the principle of angle of incidence equals angle of reflection. Therefore contrast of the pattern varies with camera angle, with camera locations closer to the angle of reflection seeing greater light intensity than camera locations farther from the angle of reflection. For wrinkled membrane surfaces in which the normal direction to the surface varies with location on the membrane, pattern contrast not only varies with camera angle, but also with target location yielding a set of images with non-uniform contrast in each individual image and also across other images.

Figures 18 and 19 show a test preformed to demonstrate the contrast challenges associated with using dot projection to measure highly reflective membrane surfaces versus diffuse white surfaces. Figure 18 shows the setup used to compare the reflective surface of an aluminized wrinkled Kapton membrane with the matte white surface of Vellum. A dot pattern was projected onto the area indicated and was imaged by a camera at multiple shutter speeds. Figure 19 shows the images generated at three different exposure times.

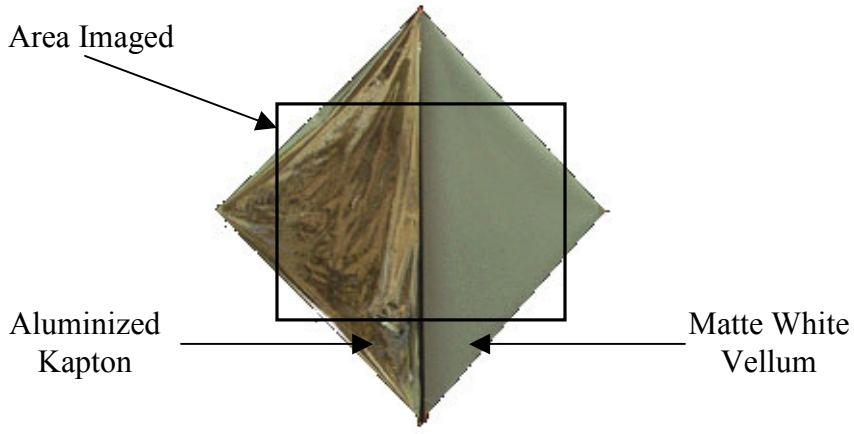

Figure 18 – Target contrast comparison test

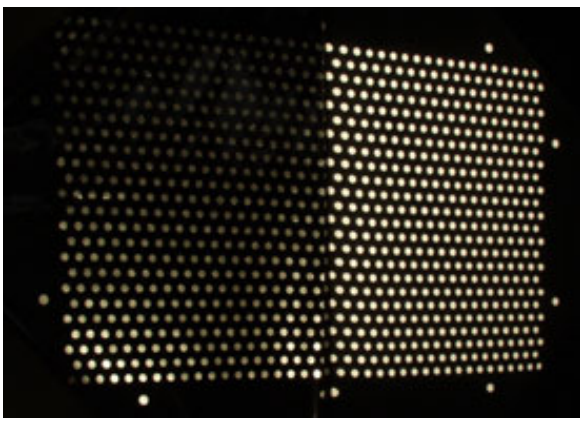

(a) 2.5 second exposure

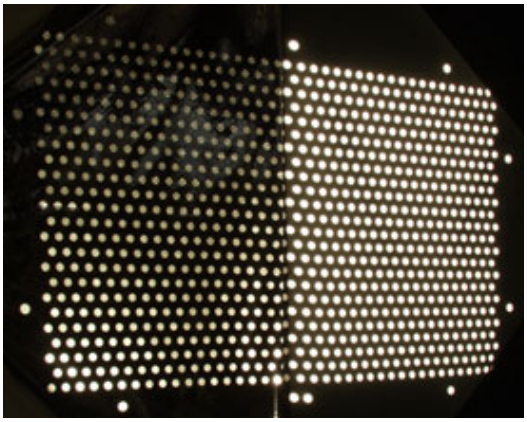

(b) 10.0 second exposure

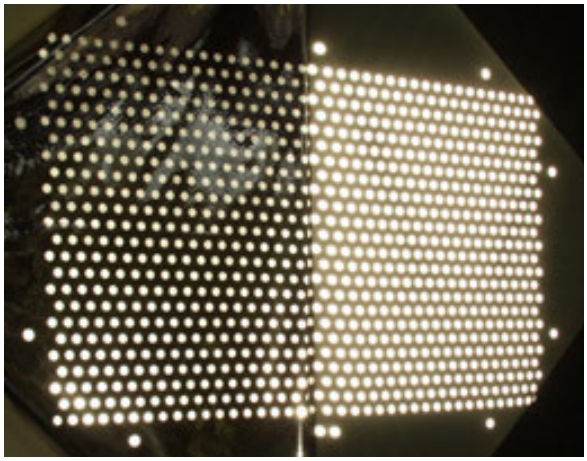

(c) 30.0 second exposure

Figure 19 – Comparison of multiple exposure times using dot projection

All of the images in Figure 19 display the non-uniform contrast gradient that occurs when photographing the Kapton membranes, shown on the left, as well as demonstrating the necessity for long exposure times. The image in Figure 19(a) has sufficient contrast in the Vellum membrane to make the photogrammetric measurements at exposure times of just 2.5 seconds compared to the 30 second exposure time in Figure 19(c) to generate adequate contrast in the Kapton sail. Also evident in the lower left corner of Figure 19(c) are the hot spots created by membrane curling. The long exposure times, contrast gradients, and hot spots will be discussed in greater detail in Chapter 7.

Another complication associated with dot projection occurs in the area of dynamics. In the case of retro-reflective targets attached to the object, dynamic data can be generated for specific object points as well as the object as a whole. Attached targets allow three-degree-of-freedom tracking, meaning that each target can be tracked in the x, y, and z directions. When using dot projection, however, the projector and therefore the pattern, remain stationary. Projected targets on a moving structure can only displace along the rays of light, either towards or away from the projector, making in-plane motion nearly impossible to characterize. However dot projection does measure the correct shape of the structure at each instant of time, even though it cannot follow specific object points. This type of point movement (only along the rays of light) implies videogrammetry using dot projection is very similar to laser vibrometry measurements (see Chapter 8), which will be used as a standard against which the videogrammetry results are compared.

7. STATIC SHAPE MEASUREMENT EXAMPLES

The three measurement examples discussed in this chapter were conducted for dual purposes: to develop measurement methods suitable for use on actual solar sail spacecraft and to obtain measurements for validation of structural analytical models. The experiments used low-fidelity, generic solar sail test articles currently at NASA Langley Research Center. These low-fidelity test articles are sub-scale models manufactured from solar sail quality materials but are not directly scalable to full size solar sails. The developed methods will be applied to other current and future high-fidelity gossamer test structures and space missions.

The first example is a low density full-field measurement of the test article, the second is a high resolution measurement of the wrinkle pattern of a small section of the sail, and the final example is full-field high resolution test to simultaneously characterize the wrinkle pattern of the sail as well as a large amplitude global deformation.

7.1 Low Density Full-field Two Meter Kapton Solar Sail

The experiment described below was designed to assess the feasibility of using projected circular targets instead of attached retro-reflective targets on highly reflective membrane surfaces. It was intended as a demonstration of the technique and was not expected to generate a high resolution characterization of surface details.

7.1.1 Test Setup

The two meter per side, square, aluminized Kapton solar sail test article shown in Figure 20 was selected for static shape measurement because of its continuity (other test articles are divided into four quadrants and do not have steady-state wrinkle patterns).

The Kodak Ektagraphic projector (Figure 11(a)) created a pattern of approximately 400 dots and four Olympus E20n cameras shown in Figure 9(a) (f/9.0, no sharpening) at approximately 90^{o} separation at the corners of the sail simultaneously photographed the sail, as shown in Figure 21. Four synchronized cameras were used instead of a single roving hand-held camera to avoid possible membrane movement between images.

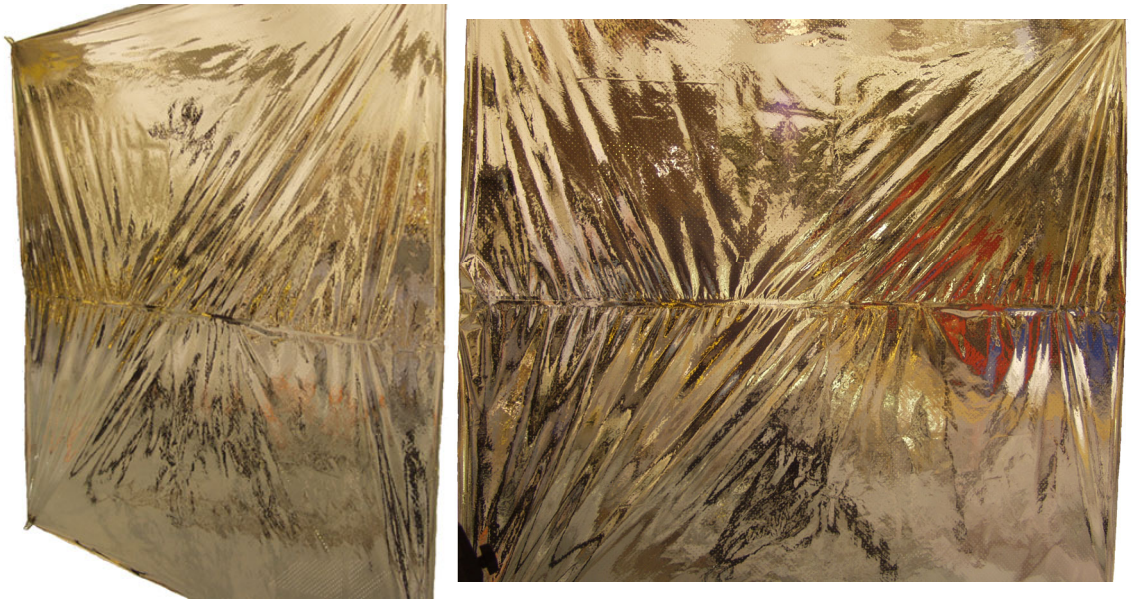

Figure 20 – Two meter Kapton solar sail test article

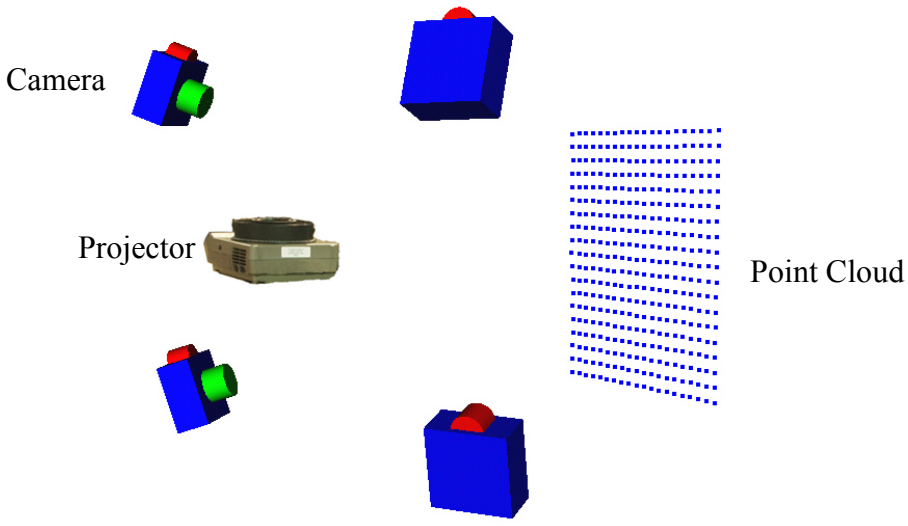

Figure 21 – Kapton two meter full field test setup

7.1.2 Images

Figure 22 shows actual images used in the photogrammetric processing, with the dot pattern clearly visible on the surface of the sail. The images are underexposed to create high-contrast targets discussed in Chapter 3.

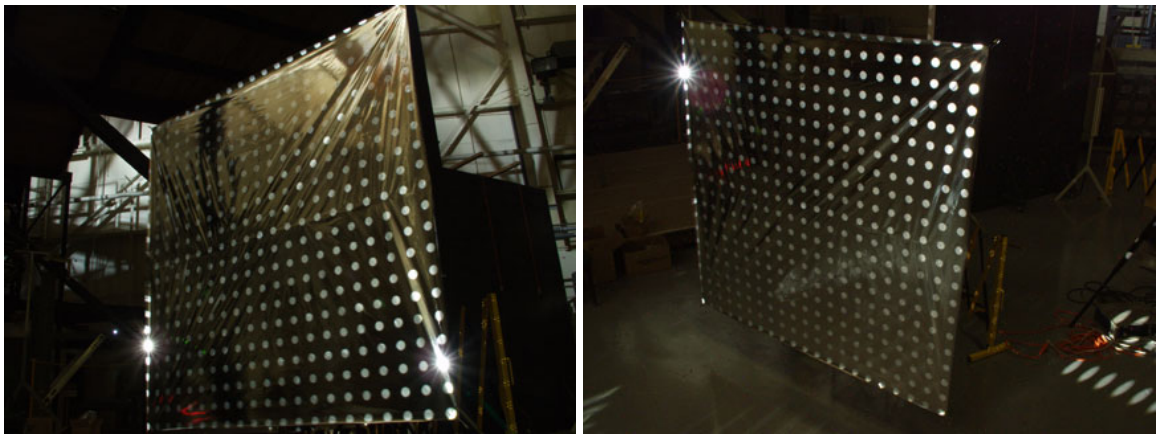

Figure 22 – Images used in photogrammetric processing (2 of 4)

Several trouble spots are evident in the images in Figure 22. The long exposure time (30 seconds) required to obtain the images due to the reflective nature of the membrane allowed ambient light to also image on the sail, causing the background to appear much brighter than desired. In the left image of Figure 22, ambient light imaging on the upper right corner of the sail drastically reduced the contrast between the dots and the membrane in that area, leading to a loss of target information. Also, there are several "hot spots" in areas where the sail curled, reflecting much more light into the camera than in the rest of image and washing out all data (i.e. targets) in that particular region. Two hot spots due to edge curling are visible in both bottom corners of the image on the left and another is visible in the upper left corner of the image on the right. The low density of the dot pattern creates a low resolution measurement condition, meaning only the overall shape and not the intricate wrinkle pattern seen in Figure 20 can be adequately characterized from these images. While the long exposure time, hot spots, and low

resolution do not preclude measurement, they detract from the achievable accuracy and precision of the process and will be addressed in the application discussed in Section 7.2.

7.1.3 Photogrammetric Processing

Figure 21 shows an image of the point cloud and camera locations created from the 3-D Viewer in the photogrammetry software, which can be studied to verify that the project processed correctly and that the setup and result are as expected. The four camera stations (one in each corner of the sail) and the final point cloud are positioned as expected. This result demonstrates that the four camera positions have been resected successfully and that the point location calculations have produced a nearly planer three-dimensional cloud, expected when measuring a predominantly flat membrane.

Figure 23 demonstrates how the imperfections in the images in Figure 22 affect the photogrammetric processing of the project. It shows a close up view of the upper right corner of the sail in the left image of Figure 22 after the processing was completed.

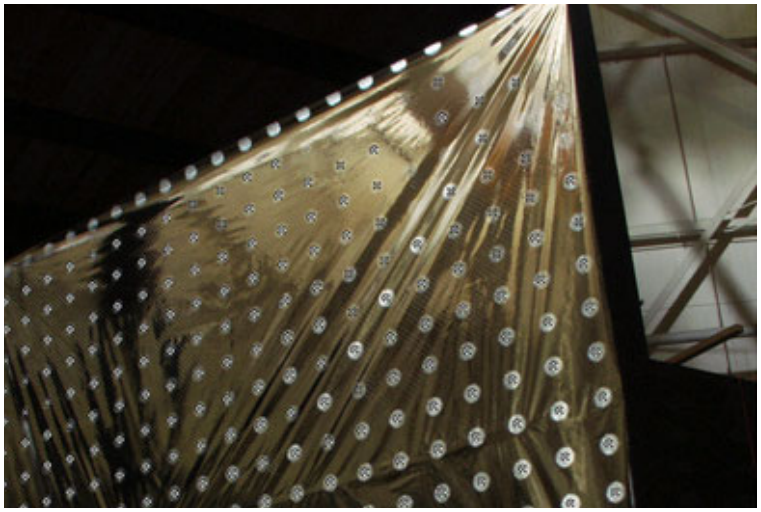

Figure 23 – Marked points in upper right corner of the solar sail test article

As discussed earlier, the ambient light in the room led to a loss of data in this region of the membrane. Some targets in the area are not visible and therefore could not be

marked. Several other targets do not have sufficient contrast to be marked using the automatic LSM process and therefore were marked by hand, reducing precision. The greatest amount of wrinkling occurs at the corners of the membrane making them important in the measurement. The ambient light, therefore, has caused a loss of accuracy and data in one of the most critical areas of the sail.

7.1.4 Error Estimates

The error estimates, discussed in Chapter 5, calculated by the photogrammetry software for this application are listed in Table 4 below. The largest residual is an estimation of the accuracy of the project. Residuals less than one pixel are considered acceptable error for the highly reflective membranes discussed here. In this application, due to the low contrast and marking of several of the targets by hand, the largest residual was quite high at 4.8 pixels, and only 63% of the points were accurate to less than one pixel residual. The average of all the precision values for all of the points in the project was calculated to be 0.16 mm, meaning that overall for the two meter sail, the measurements were precise to 1:12,500. Despite the faults in the images, reasonable data were still obtained; however the residual and precision numbers do suggest that a great deal of improvement is possible. Methods for obtaining such improvements will be shown in Section 7.2.

Table 4 – Photogrammetric error estimates

Largest Residual	4.8 pixels
Points below 1 pixel residual	63.0%
Average Precision (mm)	0.160
Precision (parts per unit object size)	1:12,500

7.1.5 Results

The coordinates of the three-dimensional points (point cloud) corresponding to centers (centriods) of the targets were exported for measurement. These data were imported into a contour mapping program, which was used to visualize the membrane shape. The first step in the visualization involves the creation of a continuous surface from the imported, discrete data – a process called gridding. A grid consists of a set of the maximum number of uniformly spaced points creating the continuous surface that do not exceed a 100 x 100 matrix. Several different algorithms may be selected by the user to create the grid, depending on the amount of smoothing and interpolation desired. The default method is a Kriging algorithm that follows trends in the data creating ridges and valleys instead of bull's-eyes around higher points and holes around lower points. The Kriging algorithm is a natural choice for displaying wrinkle patterns and was used to grid the data in Sections 7.2 and 7.3. For the low-resolution condition here, however, a Local Polynomial gridding algorithm was selected. The Local Polynomial method uses a weighted least squares fit around each inputted point, creating a series of small, joined surfaces instead of a single continuous surface. This algorithm produced better results than the Kriging for the mostly planar data gathered here. Subsequently the grid can be displayed in a variety of different plots, some of which are shown below. [32]

The results of the mapping for the gathered photogrammetry data are shown in Figure 24. The contour plot and contour surface show the overall low-resolution shape of the membrane. These types of surface measurements are useful for assessing the overall shape of the structure (e.g. is it warped or flat), but are of little value for characterizing wrinkle patterns, which requires high-resolution data. However this experiment does demonstrate the feasibility of using non-contact dot projection photogrammetry to obtain

surface shape models of highly reflective aluminized membranes. A test to measure wrinkle pattern and amplitudes of this same test article is detailed in Section 7.2.

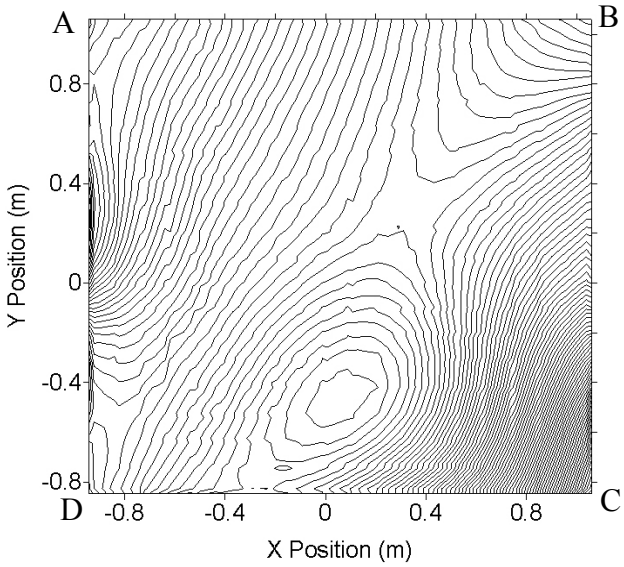

(a) Contour map

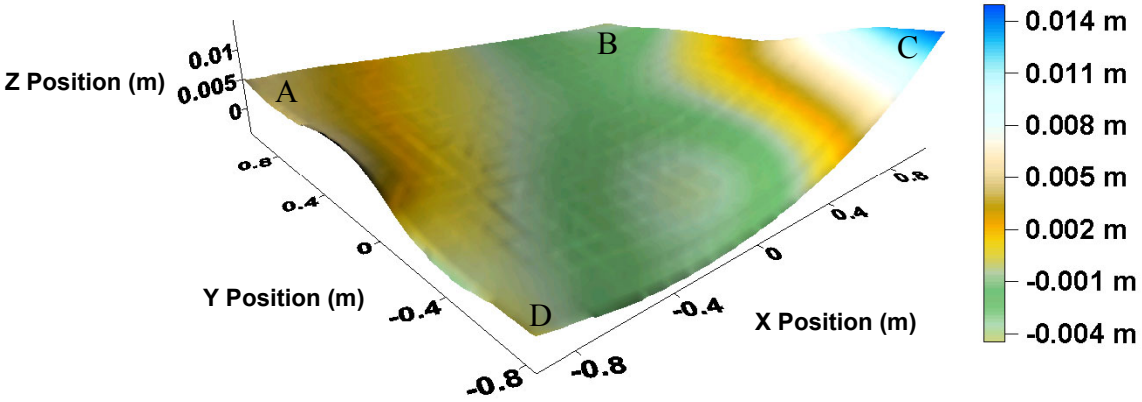

(b) Contour surface (Z Position amplified)

Figure 24 – Results for low density measurements of the solar sail test article

7.2 Wrinkle Test of Two Meter Kapton Solar Sail

The wrinkle test described here was performed to investigate if dot projection photogrammetry could successfully characterize small amplitude surface features on highly reflective solar sail membranes. Such data are important for validation of analytic structural models and will lead to better prediction of the contribution of wrinkling to loss in propulsive efficiency, to predicting and preventing localized hot spots, to understanding membrane dynamics, and to providing an indication of the corresponding film stress.

7.2.1 Test Setup

The same two meter aluminized Kapton solar sail test article used in Section 7.1 and shown again in Figure 25 was selected.

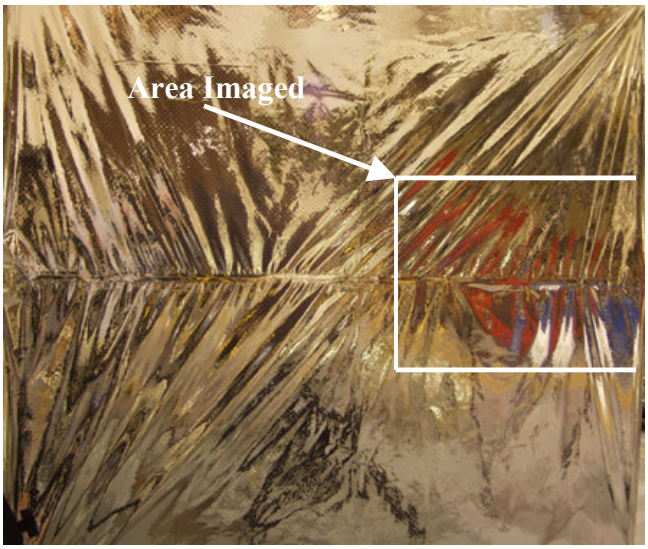

Figure 25 – Two meter Kapton solar sail test article

The observed wrinkle pattern is a complex phenomena significantly affected by the seam running across the middle of the membrane, discrete corner loads, and gravity. The pattern is marginally stable, changing somewhat with small external disturbances such as

slight air currents. To obtain a consistent set of images, the four cameras were again fired simultaneously freezing the shape. Using traditional attached retro-reflective targets in this application is clearly inappropriate.

The theater version of the Kodak Ektagraphic projector (Figure 11(b)) was used to create a grid of approximately 5100 dots on a 0.9 x 0.5 meter area on the right side of the sail, as indicated in Figure 24. The same four Olympus E20n cameras (Figure 9(a)) used in Section 7.1 arranged in the same configuration, one in each corner, simultaneously photographed the grid (f/9.0, no sharpening) instead of a single roving camera, again done to eliminate the chance of inadvertent membrane movement. The reflectivity of the aluminized coating of the Kapton that led to the use of long exposure times in Section 7.1 was again a complicating factor, but was compensated for much more effectively. The higher powered projector and smaller distances involved allowed exposure times below 30 seconds, and the cameras were set to identical exposure values instead of the identical shutter speeds used previously. The exposure value, which indicates the over- or under-exposure of the image, of –1.0 set different shutter speeds in each camera ranging from 15 to 30 seconds, resulted in images of similar contrast.

7.2.2 Images

Two of the images used in the processing are shown in Figure 26. The images are nearly optimal white-on-black images. Ambient room lighting has been eliminated and while the contrast gradient is still present, each image contains useful data out to the corners of the projected pattern. Note that while hot spots still caused a loss of data in the image on the right, the nearly uniform contrast in all of the images enabled redundancy

that minimized the negative impact of the hot spots on the final outcome. In general the location of hot spots varies from one image to the next.

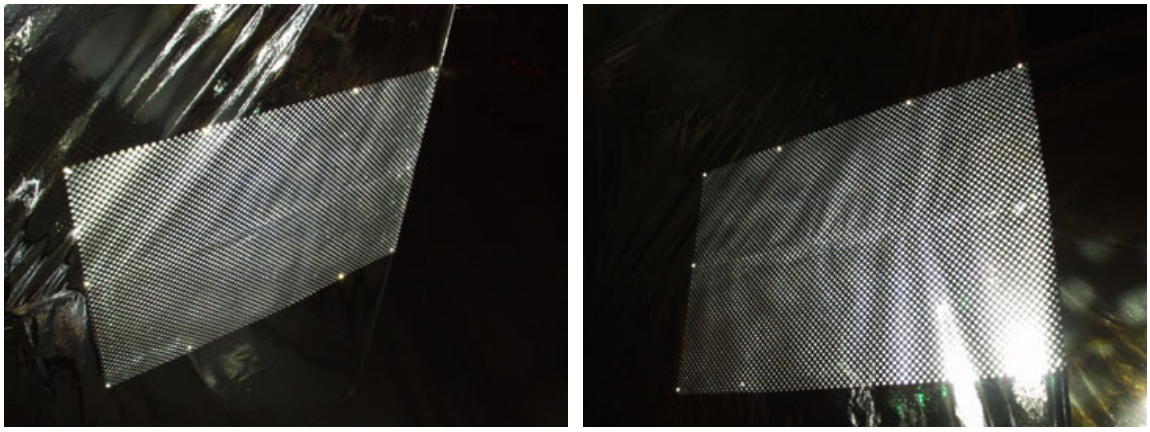

Figure 26 – Images used in photogrammetric processing (2 of 4)

7.2.3 Photogrammetric Processing

Figure 27 shows an image of the completed project created with the 3-D Viewer in the photogrammetry software. The graphic shows the camera stations at approximately 90^{o} angles of separation, their relative orientations and fields of view, and the final point cloud, all appearing as expected. Figure 28 is a magnified view of the upper left corner of the grid visible in Figure 26, after the target marking was completed. Evident is a higher resolution compared with the data in Section 7.1, indicating that the data points are sufficiently dense to measure the visible wrinkles. The greater density, however, does have a drawback; it is highly computationally and labor intensive to calculate the positions of over 5000 points. The measurement in Section 7.1 required hours to process, while this measurement required almost one week (8 hours computing time on a 2.0 GHz processor, 30 hours data handling). Also apparent in Figure 28 is that sufficient contrast existed for the computer to accurately mark the centers of almost all the targets using LSM centroiding. Automatic centroiding minimized the need for the

human intervention necessary in Section 7.1, thereby maximizing the accuracy of the marking process. The increase in the total time required to process the data resulted from the need to iterate on the solution. The automated functions in the photogrammetry software required multiple adjustments and corrections that were not necessary in the previous measurement example.

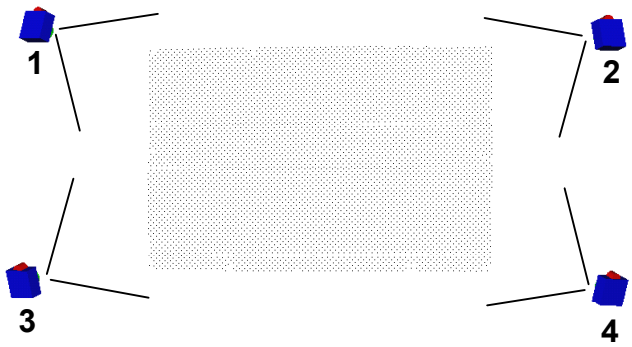

Figure 27 – Camera locations with fields of view

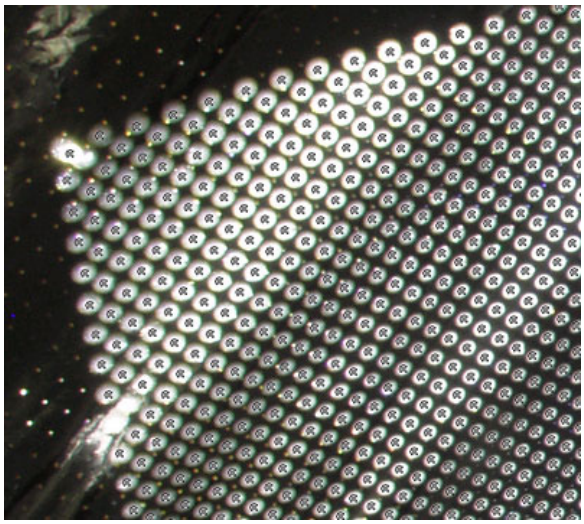

Figure 28 – Marked points in upper left corner of the area imaged

7.2.4 Error Estimates

Table 5 contains the estimated error quantities calculated by the photogrammetry software for this test along with those for the test described in Section 7.1. The largest

residual from all 5000 points is only 1.8 pixels, and over 98 percent of the points are below a 1.0 pixel residual, giving high confidence that the measurements are accurate. The average precision was calculated to be 0.062 mm, yielding an overall precision on the area measured of 1:32,300. These numbers, combined with the high target density, allow for accurate measurement of wrinkles less than one millimeter in amplitude.

Table 5 – Comparison of two photogrammetric error estimates

Experiment in:	Section 7.1	Section 7.2
Largest Residual	4.8 pixels	1.8 pixels
Points below 1 pixel residual	63.0%	98.9%
Average Precision (mm)	0.160	0.062
Precision (parts per unit object size)	1:12,500	1:32,300

Table 5 shows that the measurements in this section are a marked improvement in measurement residuals and precision over Section 7.1, demonstrating for the first time that high quality, high-resolution measurements can be obtained for these structures using dot projection photogrammetry. Improvements in hardware and technique led to the gains, and further advances, detailed in Section 7.3, will produce still better measurements.

7.2.5 Results

A contour map (Figure 29(a)) and a shaded relief map (Figure 29(b)) were created using the exported 3-D coordinates from the photogrammetric process. These maps, normally used for displaying topographic land features, clearly characterize the visible wrinkles in the Kapton membrane and the seam cutting horizontally across the center. The wrinkle amplitude can be determined in Figure 30 by examining the two views of the

contour surface. The smallest wrinkle amplitude is approximately 0.25 mm and the average wrinkle amplitude is approximately 5.0 mm. The seam and wrinkles of the membrane are clearly visible in these results and match the pattern seen in Figure 25. Note the amplitude in the Z-direction has been exaggerated for better viewing.

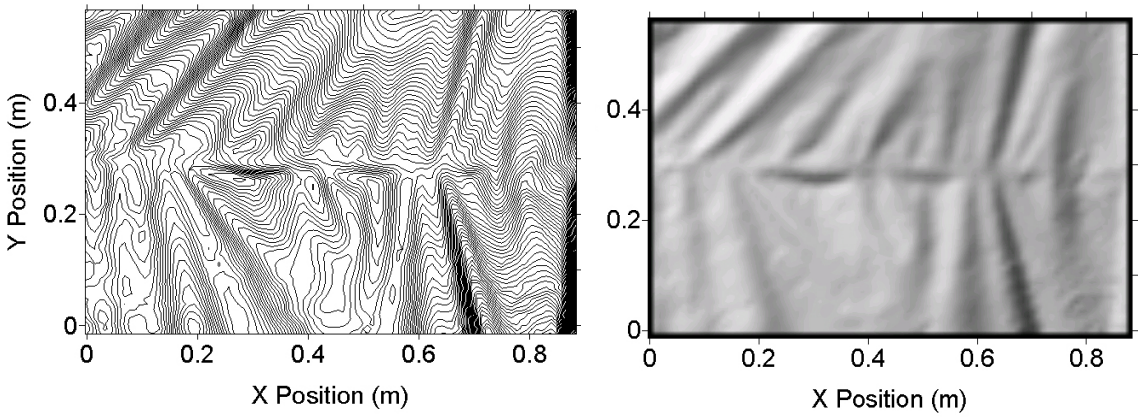

(a) Contour map (b) Shaded relief map

Figure 29 – Results for wrinkle measurement of the solar sail test article

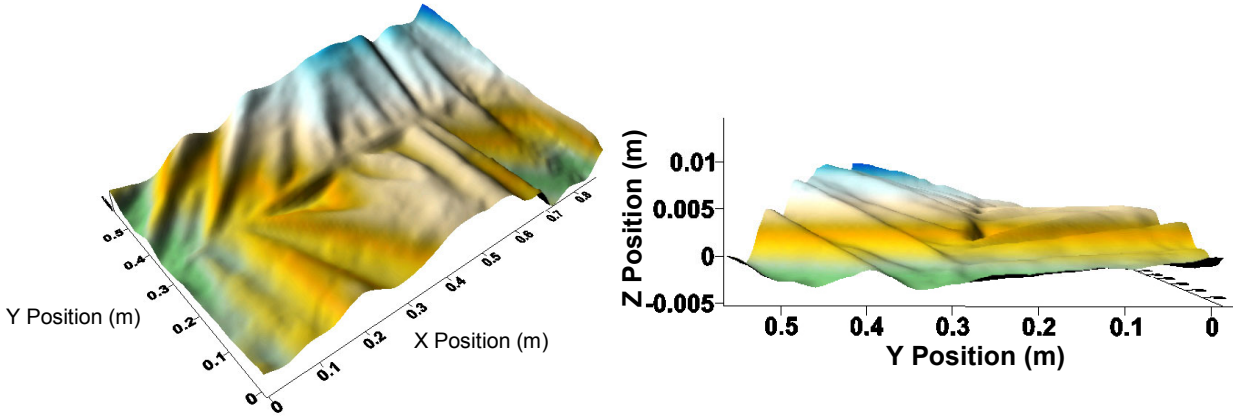

Figure 30 – Two views of contour surface

These results demonstrate that it is possible using careful experimental technique to make non-contact photogrammetric measurements of highly reflective membranes that accurately characterize their static shape, including wrinkling. These measurements are the first of sufficient quality to validate analytical models of this configuration. More powerful projectors will allow high-resolution measurements such as these on even large gossamer structures.

7.3 High Density Full-field Two Meter Kapton Solar Sail

The high density full-field test described here was designed to generate measurements of comparable resolution to the results in Section 7.2 over the entire surface of the two meter Kapton solar sail instead of over only a small section. It was intended to demonstrate the ability of dot-projection photogrammetry to simultaneously characterize medium-amplitude wrinkles and large-amplitude surface features.

7.3.1 Test Setup

The same square two meter Kapton solar sail test article was used once again, however, it was rotated slightly, as shown in Figure 31, to create a slight billow in the bottom half of the membrane to demonstrate the ability of the method to simultaneously measure both medium-amplitude wrinkles and global non-planar shapes. Four Kodak DCS 760M cameras (Figure 9(b)) again at 90^{o} angles of separation at the corners of the membrane photographed (f/11.0, no sharpening) a grid of approximately 10,800 targets created by the GSI ProSpot (Figure 11(c)) flash projector. The use of the Kodak cameras and the ProSpot projector signify a transition to professional grade hardware, as stated in previous chapters, to yield full-field, high-resolution, high precision measurements of currently available two meter solar sail structures. To the extent possible NASA will apply these methods to even larger solar sail scale models (10 m and 20 m) to be manufactured in the near future. Experimental methods developed here will be used and possibly extended further as required.

Figure 31 – Two meter Kapton solar sail test article rotated slightly with billow

7.3.2 Images

Two images used in the photogrammetric processing are shown in Figure 32. As discussed in Chapter 3, the images are monochromatic and underexposed. Ambient room lighting was minimized, but data was still lost due to the intensity of the flash projector. Because of the billow in the sail and the angles involved, a percentage of the light reflected by the membrane fell onto the floor. The high intensity of the projector meant a large amount of light, when scattered in all directions by the floor, imaged back onto the membrane. These images of the light on the floor were of sufficient intensity to wash out the original points. This loss of data will be discussed further in Section 7.3.3. Curling of the membrane and the large distances involved again led to hot spots in the images;

however the loss of data at these points was compensated for again by the redundancy of four cameras.

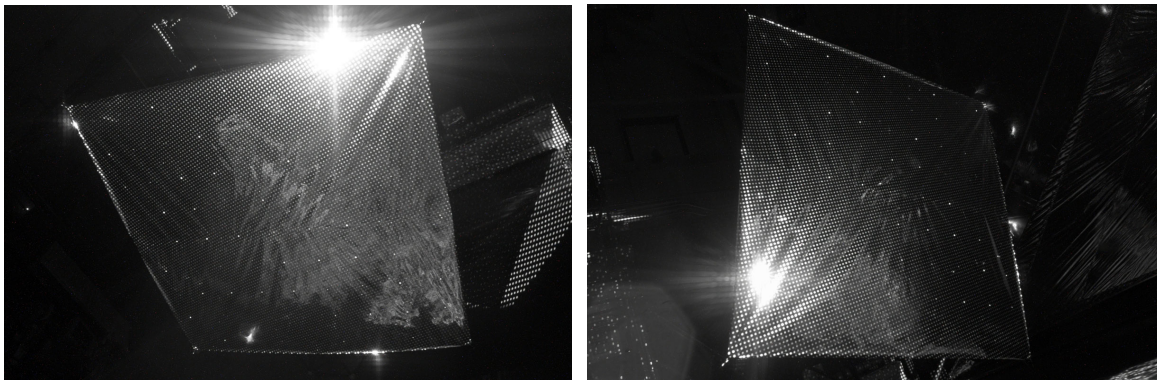

Figure 32 – Images used in photogrammetric processing (2 of 4)

7.3.3 Photogrammetric Processing

A three dimensional point cloud similar to those seen in Figures 21 and 27 in Sections 7.1 and 7.2 again resulted from the photogrammetric processing. The time required to generate the final project, however, was much greater than in the two previous examples. The measurement in Section 7.2 required 8 hours of computer time and 30 hours of data handling whereas this project required approximately 90 hours on a 2.0 GHz processor and an additional 80 hours of data handling. The current photogrammetry software was not designed to process such a large number of points, over 10,000 in this measurement, or to handle such close point spacing. The loss of data caused by hot spots and the image of the floor, shown in the top portion of Figure 33(a), added to the overall complexity of the processing, making this an extremely demanding and complicated measurement. Figure 33(b) shows how the redundant use of four cameras allows for useful data to still be gathered from this area. A combination of the four cameras effectively cover the region and yield useful data (each target must be marked in at least

two images to be located in 3D space). Also evident in Figure 33 is the ability of the software to mark the projected dots using the LSM centroiding, as well as the true resolution of the projected pattern (impossible to see in Figure 32). In this case, the number of dots per square meter is nominally half as high as that used for the measurement in Section 7.2, but it is the highest currently achievable with the available hardware. Note the highest density Pro Spot slide projects 22,500 targets in a circular pattern. The position and shape of the test article dictated that for full coverage of the sail, only a portion of targets could be used. Approximately 10,800 dots were projected onto the membrane, and with the small size of the targets and the distance from the test article to the cameras (approximately three meters), some dots appeared as small as five pixels in diameter with as little as five pixels spacing. Higher pattern resolution or larger dots are therefore impractical for this measurement given the current hardware configuration.

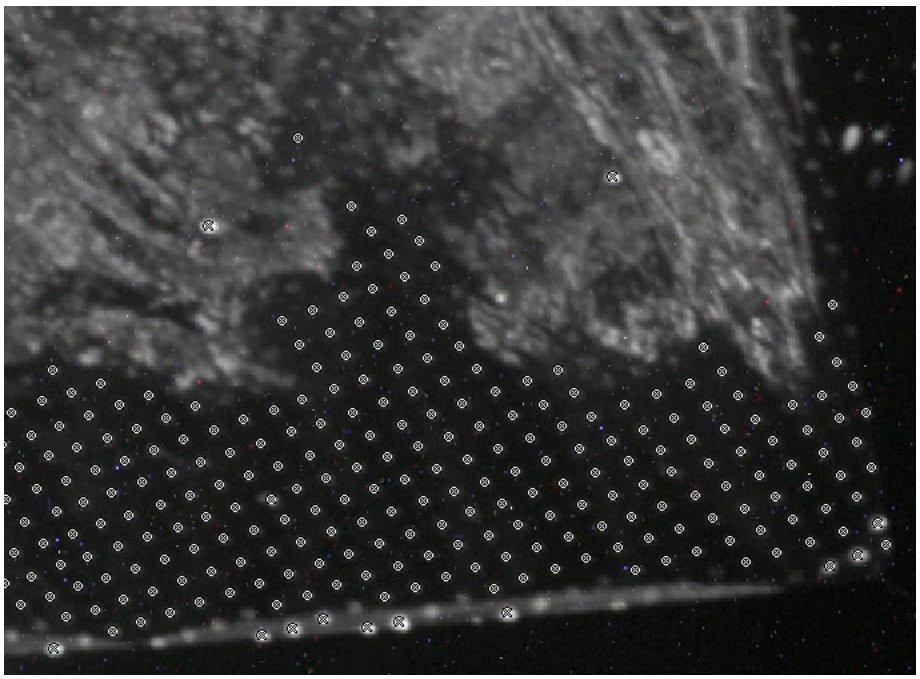

(a) Un-useable data in top half of image

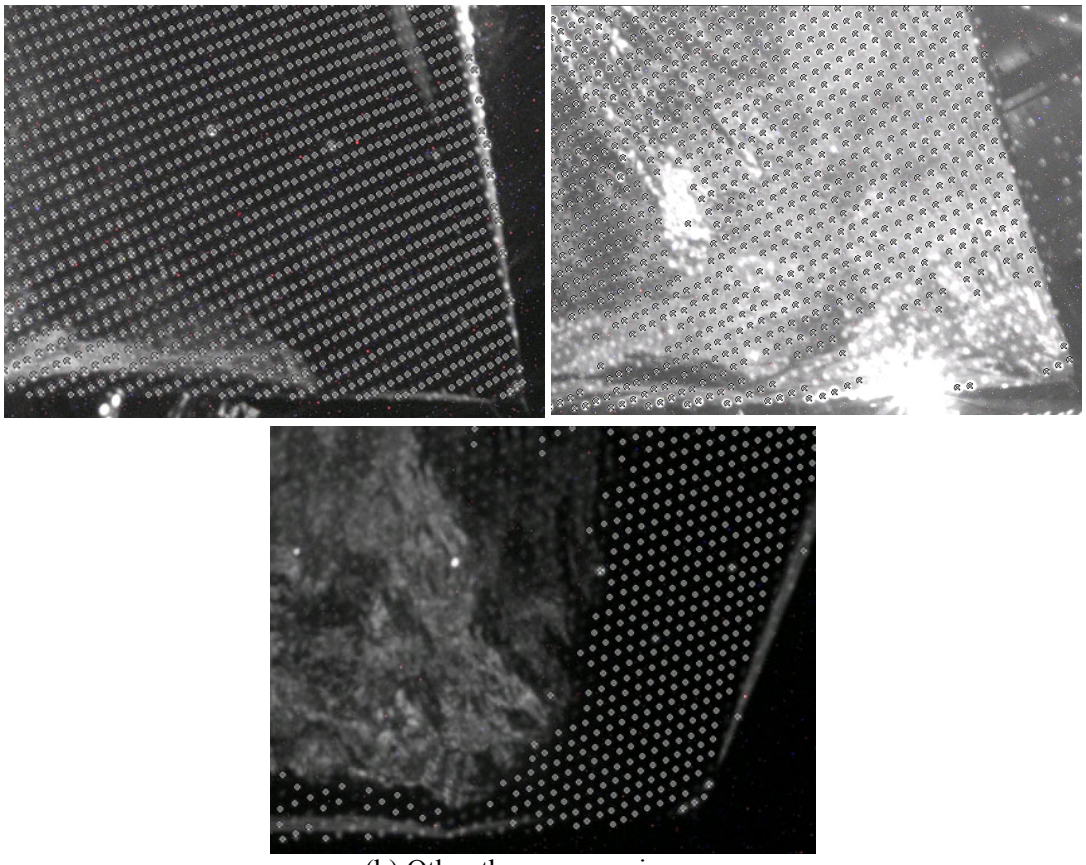

(b) Other three camera images

Figure 33 – Marked points in lower right 0.01 m^2 of solar sail test article

7.3.4 Error Estimates

Error estimates for all three static shape measurements discussed thus far are listed in Table 6. The largest residual of the above project was slightly higher than that in Section 7.2 and can be explained by the relatively poor quality of the data. Even with this poor quality, however, over 95% of the points had under a one pixel residual. The most important improvement of this measurement over the previous one is evident in the precision numbers. Over the four square meters of membrane area imaged, the Kodak system was precise to 59 microns versus 62 microns over less than 0.5 square meters imaged previously, meaning that the overall precision increased from 1:32,300 to 1:50,800. While this test represents another significant improvement in measurement precision, it also substantiates the principle of diminishing returns mentioned in Chapter 6. The system used in the above test relied on professional hardware costing almost ten times that of the system used in Sections 7.1 and 7.2. Combined with a significant increase in processing time, this system represents a substantial investment that only doubled the resulting measurement precision.

Table 6 – Comparison of all photogrammetric error estimates

Experiment In:	Section 7.1	Section 7.2	Section 7.3
Largest Residual	4.8 pixels	1.8 pixels	2.7 pixels
Points below 1 pixel residual	63.0%	98.9%	95.5%
Average Precision (mm)	0.160	0.062	0.059
Precision (parts per unit object size)	1:12,500	1:32,300	1:50,800

7.3.5 Results

While Section 7.3.4 provides little justification for the added cost of the professional system, the results more than compensate for the fact that the price increase

was far greater than the precision increase. The contour map and shaded relief map shown in Figure 34 clearly characterize all the medium-amplitude wrinkles, the seam, and the billow seen in Figure 31. These plots detail the entire surface of the test article instead of just a small area as in Section 7.2. Figure 35 shows two views of the contour surface generated from the data. The wrinkles are clearly evident, but in addition it is possible to see the true size of the billow compared to the wrinkles. The measured wrinkles are on average five millimeters in amplitude, matching the measurement in Section 7.2, while the billow is almost ten times that size. Also apparent in Figure 35 is the tendency of the membrane to curl at the edges.

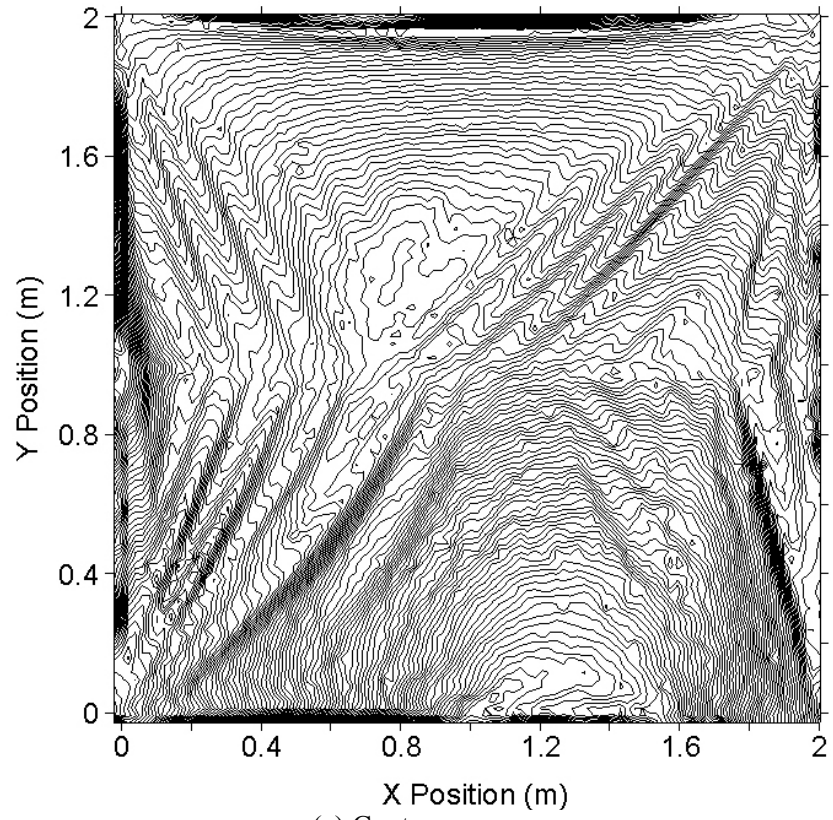

(a) Contour map

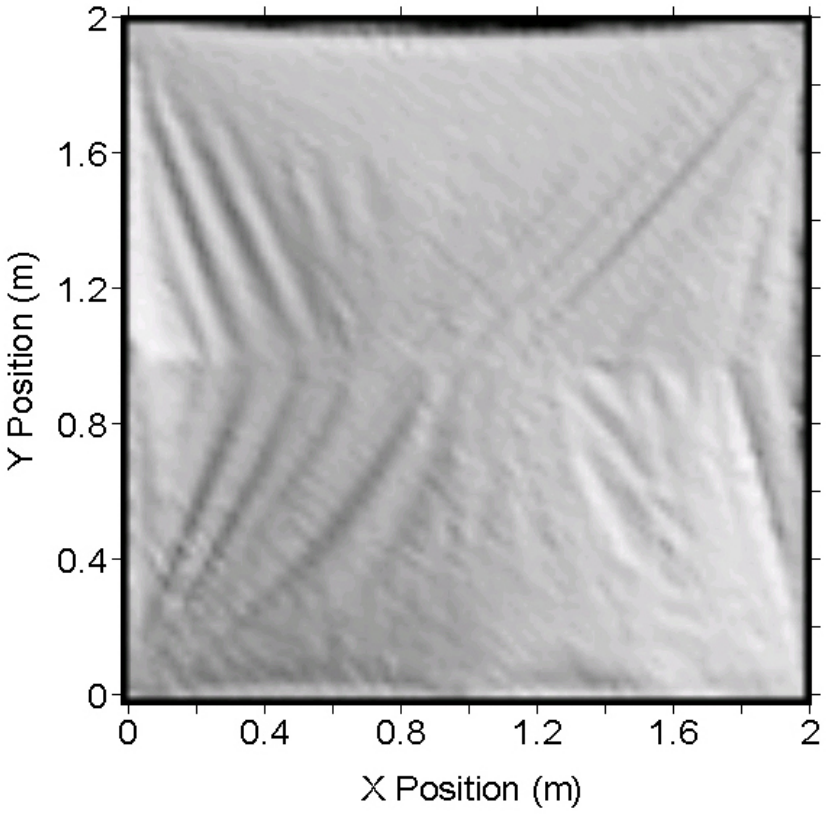

(b) Shaded relief map

Figure 34 – Results for high density full-field measurement of the solar sail test article

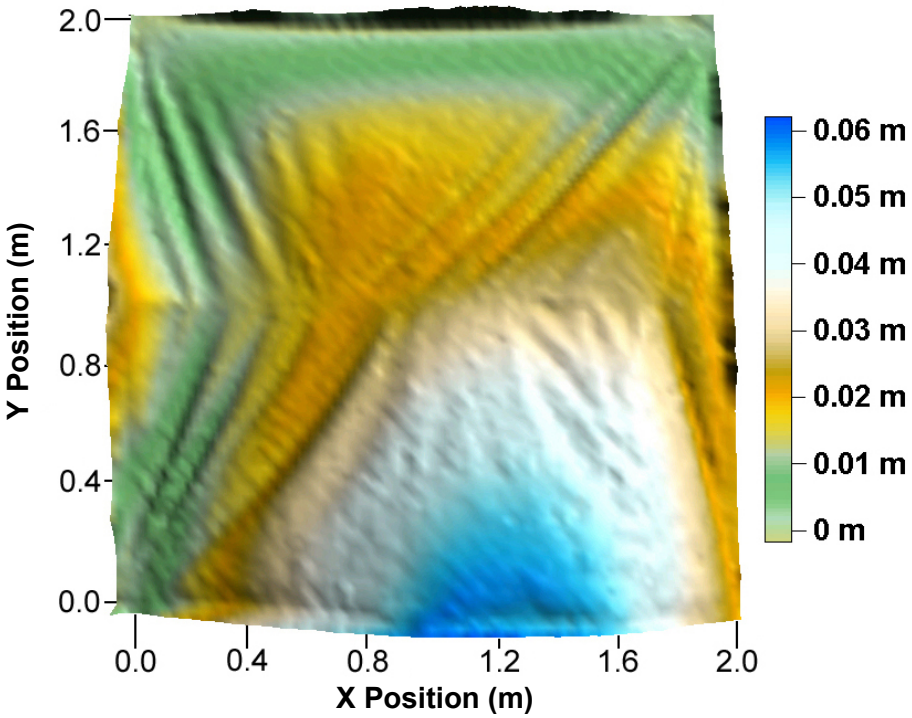

(a) Top view

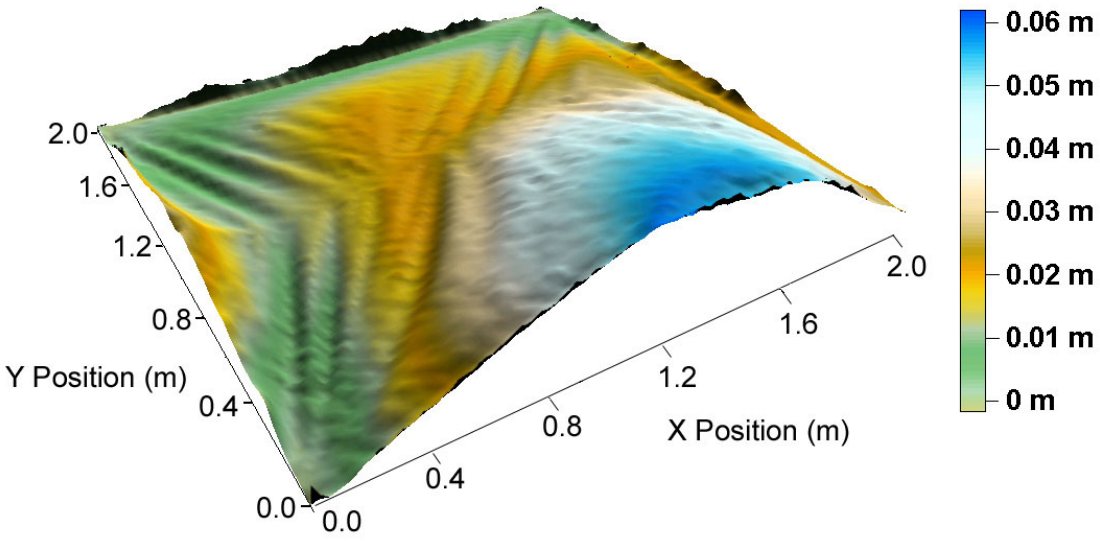

(b) Perspective view

Figure 35 – Two views of the contour surface generated

While it is impossible to obtain a quantitatively accurate comparison of the results obtained photogrammetrically to the actual shape of the membrane due to the lack of any more accurate measurement system, qualitative validation can be performed. Careful

examination of the membrane shown in Figure 31 reveals patterns of wrinkles that begin in the corners of the membrane and progress in straight lines diagonally toward the center. The same trends are visible in Figures 34 and 35. These figures also show the seam cutting across the center of the membrane visible in Figure 31. The billow occurs in identical locations in all three figures, and in the lower left quarter of the membrane the last of the wrinkles curves toward the center instead of running in a straight line. This qualitative validation combined with the maturity of the photogrammetric technique and the quality of this particular measurement gives high confidence that these results are accurate.

The shape characterization produced above is unique. A realistic solar sail model has never before been produced in a full-field, totally non-contact manner to this resolution. These surface models are of sufficient quality to be used for validation of analytical models and for supporting development of hardware and software tools for future measurements and use in space, achieving both of the goals expressed prior to Section 7.1.

8. DYNAMIC ANALYSIS OF A TWO METER VELLUM SOLAR SAIL

Structural dynamic characterization is also important for the development and validation of analytical models supporting future designs of gossamer structures in general and solar sails in particular. In the dynamic analysis of these structures, as in the static characterization, non-contact measurement is necessary to avoid altering the responses of the objects being measured. Videogrammetry, discussed in Chapter 3, expands the methods and techniques of photogrammetry to multiple time steps yielding dynamic data. While other non-contact dynamic measurement techniques exist, they are not full-field. It was hoped that the dynamic data generated would be useful in simply tracking the overall shape of the membrane as a function of time. The accuracy of the measurement of the resonant frequencies and operating deflection shapes that were extracted, however, surpassed expectations.

8.1 Test Setup

Figure 36 shows the two meter solar sail test article measured in this application. The test article membranes are 100 micron thick (thinnest commercially available) Vellum, a diffuse white material ideal for dot projection since it scatters light almost equally in all directions regardless of the angle of incidence. This property enables the Vellum to yield a grid of uniform contrast from any camera angle. The test article is not designed to approximate actual solar sail material as is the test article used in the first three applications, but is designed as a research tool for measurement method development. Figure 37 shows the test setup used in the experiment. A grid of 49 dots was created on the right quadrant of the four quadrant solar sail by the digital projector shown in Figure 11(d) and retro-reflective targets were attached to the booms. A long-

stroke electrodynamic shaker attached to the tip of the lower right boom excited the structure with a pseudo-random forcing function. A scanning laser vibrometer measured the frequency response function of the sail quadrant and its corresponding operating deflection shapes, and is used below as a standard against which to compare and determine the validity of the videogrammetry results.

Figure 36 – Two meter four quadrant Vellum solar sail test article

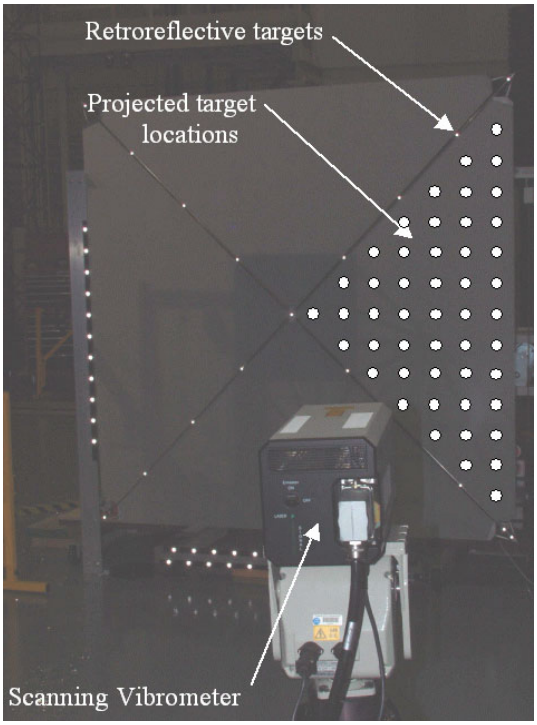

Figure 37 – Test setup for dynamic characterization

8.2 Measurements

The scanning laser vibrometer system is an industry standard for determining modal frequencies and shapes of structures. The user defines a measurement grid – in this case the same grid used in the videogrammetry – and at each point the displacement or response to an input force is measured. Using the calculated power spectral densities and cross spectral density of these input and output signals, the vibrometer software generates the frequency response function (FRF) for each measured point, as well as coherence functions, phase angles, and other modal analysis data. Relevant modal frequencies are then selected by the user – usually at peaks in the FRF – and animated by the software, as shown below. The laser vibrometer is a complete modal analysis system used for both gathering and analyzing vibration data. [33, 34]

The question then arises: if the scanning laser vibrometer is such a powerful system, why study videogrammetry? As the name implies, the vibrometer can scan or measure multiple points, but does so one point at a time. At each point the measured signal (response vs. time) is divided into blocks for each of which the software calculates a Fast Fourier Transform (FFT). Variations of this technique, often combined with windowing, are used to smooth the data. Each block is then discritized into samples depending on the desired resolution of the measurement. An artifact of the analogue anti-aliasing filter requires that the number of samples equals 2.56 times the number of FFT lines. These FFT lines define the resolution of the measurement by:

$$\Delta f = \frac{BW}{n_{FFT}} \tag{6}$$

Where Δf is the resolution, BW is the bandwidth of the measurement (i.e. from 0 to 10 Hz), and n_{FFT} is the number of FFT lines. At high resolutions, therefore, the vibrometer measures thousands of FFT lines at each point, 1600 in this application, to produce detailed results. However this form of data acquisition by scanning each point individually is slow at low frequencies, requiring several hours to run one test. Videogrammetry is attractive because of its ability to measure all of the points simultaneously. For the results presented below, the cameras recorded data for approximately 26 seconds gathering a total of only 384 frames each instead of several sets of 3200 samples (twice the number of frequency lines) taken by the vibrometer at each point. While the videogrammetric results shown below are arguably not as clean as the vibrometer data, they are full-field, simultaneous measurements taken in just a few seconds instead of hours. [33 – 35]

8.3 Results

The position versus time videogrammetry data was loaded into modal analysis software for interpretation where two different computational methods were used. The first involved overlaying the time histories of individual points and calculating the Fourier transform of the joint history. The software then animated the Operating Deflection Shapes (ODS) at each peak in the frequency domain [36]. The second method of analysis calculated frequency response functions. Here only one degree of freedom was used, the out-of-plane displacement in the Z direction, identical to that used by the vibrometer. As stated above, an FRF is calculated by dividing either the output spectral density or the cross spectral density by the input spectral density, the difference in the two methods generating the coherence function [35]. For the videogrammetry experiment the input signal was not measured, so a reference point was specified enabling the software to divide out the input and calculate the FRF's (Figures 38 and 39) and animate shapes again at the peaks in the frequency domain [37]. The combined results of both of these methods of analysis are compared against the results of the laser vibrometer measurements in Table 7 below. While neither the ODS or FRF method is currently considered to be entirely accurate, some combination of the two will likely capture all dynamics below 5 Hz [38]. Note that the non-linear nature of the deflection shapes, their coupling, and the inability to compensate for atmospheric damping mean that the shapes shown in Figures 40 through 44 are not actually mode shapes, and that the frequencies listed in Table 7 are not actually modal frequencies. These can alternatively be referred to as "structural resonances" and "resonant frequencies."

Table 7 – Identified resonant frequencies of the 2 m Vellum solar sail

Laser Vibrometer	Videogrammetry
1.75 Hz	1.77 Hz (ODS)
2.65 Hz	2.49 Hz (FRF, ODS)
	2.81 Hz (ODS)
3.34 Hz	3.28 Hz (FRF)
3.67 Hz	3.69 Hz (ODS, FRF)
4.74 Hz	4.75 Hz (ODS, FRF)

Examination of Table 7 reveals good correlation between the results found using laser vibrometry and videogrammetry. While several inconsistencies are evident, overall the modal frequencies were measured to within 0.2 Hz of each other. Figure 38 shows the overlayed magnitude of the three frequency response functions (videogrammetry ODS, videogrammetry FRF, and laser vibrometer) of a single point. It is clear how the two methods of analyzing the videogrammetry data were used in conjunction to approximate the laser vibrometer data. The first large peak in the magnitude of the vibrometer data has a corresponding peak in the videogrammetry ODS data, while the second vibrometer peak corresponds to a peak in the videogrammetry FRF. Note that while it is customary to show a phase angle plot with the magnitude plot, in this case no useful information is contained in the phase data, and it is therefore not shown. The randomness and scatter in Figure 38, even in the high quality vibrometer data, indicates a high degree of modal coupling, non-linearity, and noise present in the system.

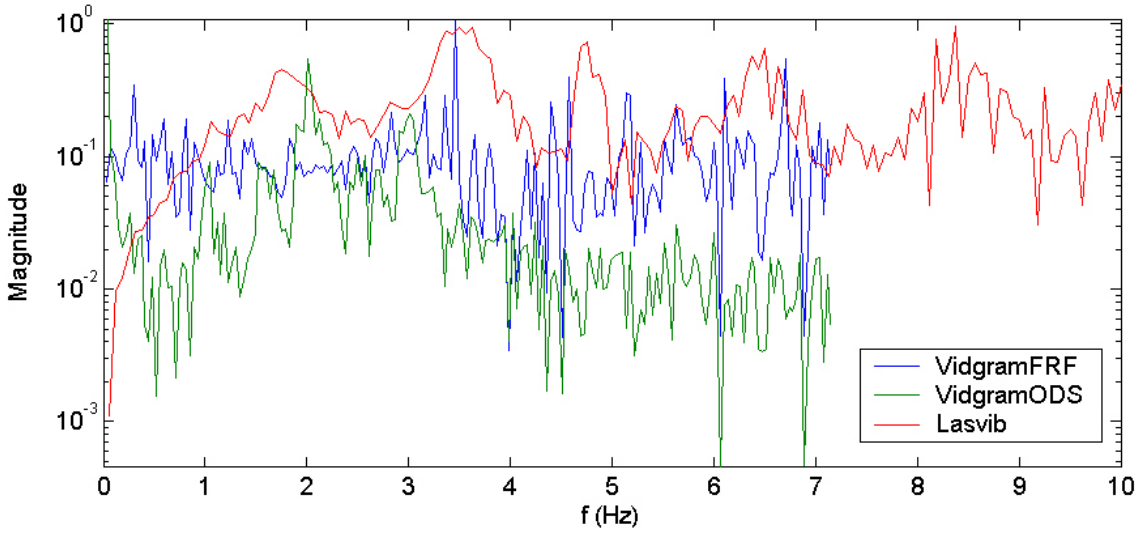

Figure 38 – Comparison of frequency response functions for a single point

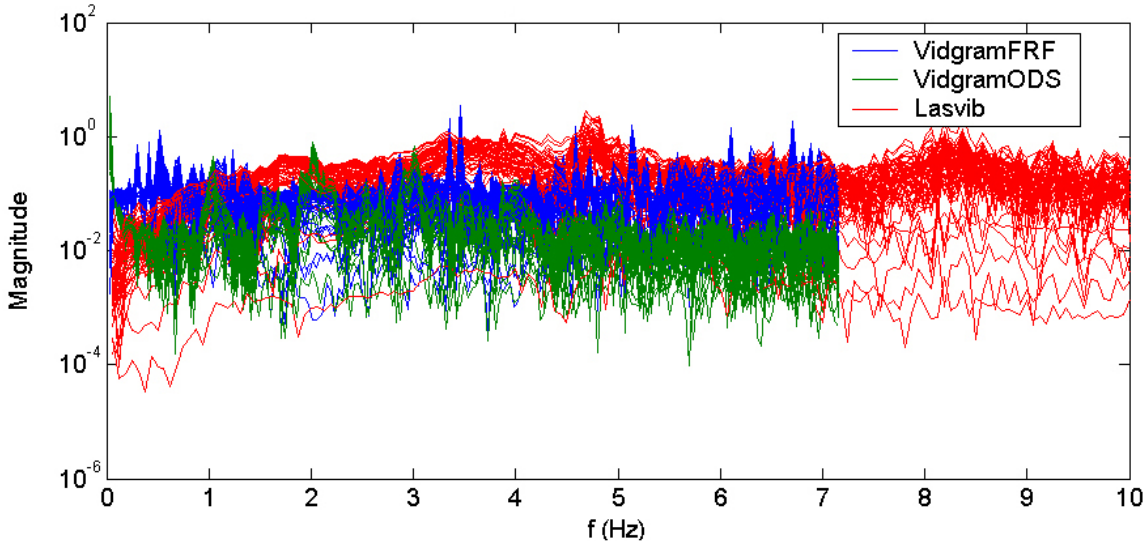

Figure 39 – Overlayed magnitudes of frequency response functions for all measured points

Figure 39 shows the magnitudes of the frequency response functions for all of the points for each of the three analysis methods. The visible scatter in the vibrometer data again indicates the complexity of characterizing solar sail structures. Also evident is the fact that peaks in one or both sets of videogrammetry data generally correspond to peaks in the vibrometer data. The frequencies listed in Table 7 were selected by analyzing the damping and the deflection shape at each of these peaks. Clean shapes and low damping

were considered to be the true structural resonance shapes and the corresponding frequencies considered to be the true resonant frequencies of the system.

Apparent in both Figures 38 and 39 is the bandwidth limitation of the videogrammetry system. While the bandwidth of the vibrometer can be customized for each scan (in this case set from 0 to 10 Hz), the maximum frequency at which videogrammetry can generate data, or Nyquist frequency, is always one half of the sampling rate. In this case the cameras ran at slightly less than 15 Hz yielding a Nyquist frequency of just over 7 Hz. Nyquist is important because recorded motion caused by modes occurring above it reflects back into the measured spectrum creating peaks at frequencies where resonance does not exist, an effect called aliasing [39]. While the laser vibrometer has anti-aliasing filters to compensate for the effect, the videogrammetry system does not. The multiple peaks below 1.0 Hz in the videogrammetry FRF are believed to have been caused by aliased boom modes. Compensating for aliasing will be a challenge for future videogrammetry work.

Figures 40 through 44 show the deflection shapes for each of the modal frequencies listed above, again comparing the laser vibrometry shapes and the videogrammetry shapes. In general, the videogrammetry shapes are noisier than the shapes obtained using the vibrometer, which is to be expected due to the disparity in data volumes, but overall there is good correlation, especially at higher frequencies.

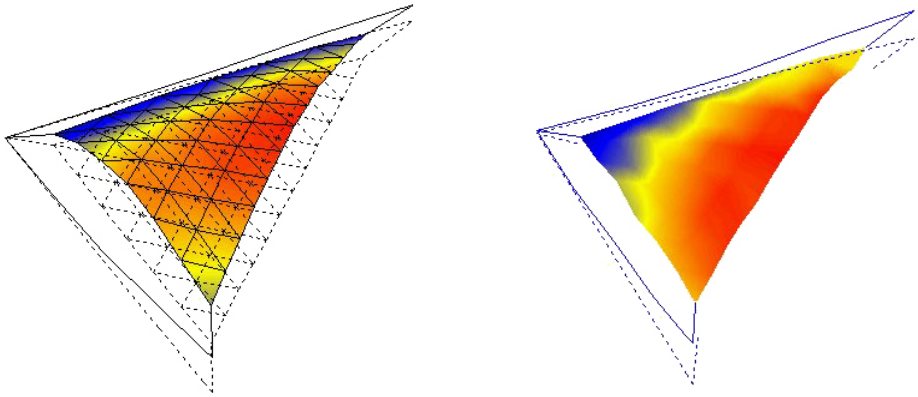

(a) 1.75 Hz Laser Vibrometer (b) 1.77 Hz Videogrammetry (ODS)

Figure 40 – First deflection shape comparison for Vellum solar sail test article

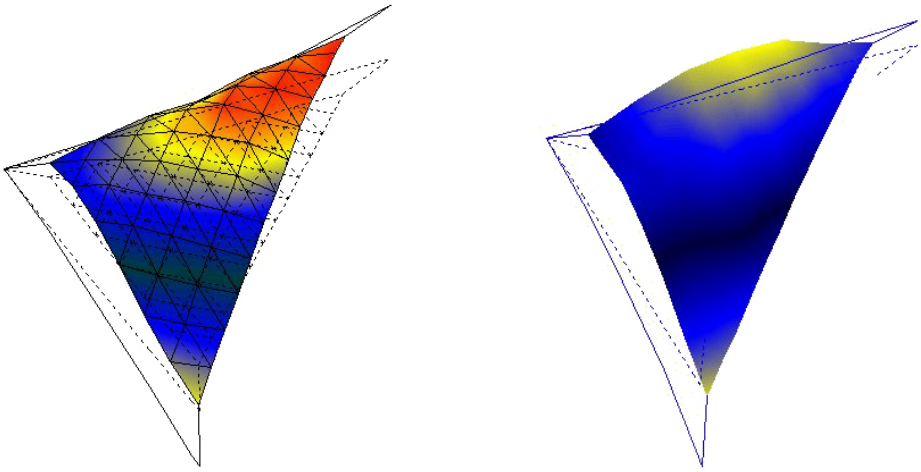

(a) 2.65 Hz Laser Vibrometer (b) 2.49 Hz Videogrammetry (FRF)

Figure 41 – Second deflection shape comparison for Vellum solar sail test article

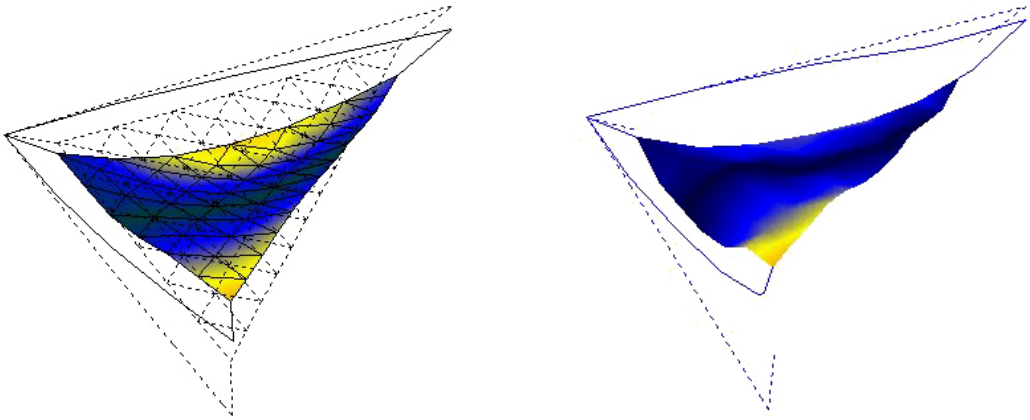

(a) 3.34 Hz Laser Vibrometer (b) 3.28 Hz Videogrammetry (FRF)

Figure 42 – Third deflection shape comparison for Vellum solar sail test article

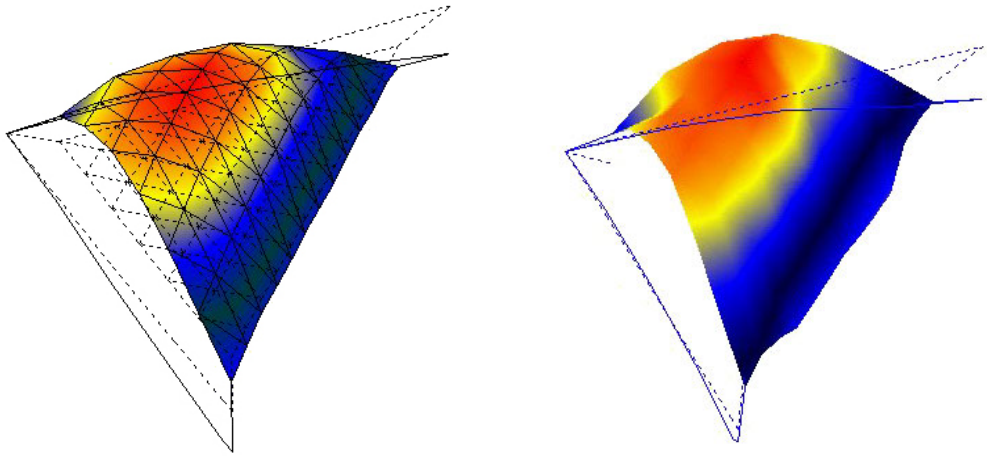

(a) 3.67 Hz Laser Vibrometer (b) 3.69 Hz Videogrammetry (FRF)

Figure 43 – Fourth deflection shape comparison for Vellum solar sail test article

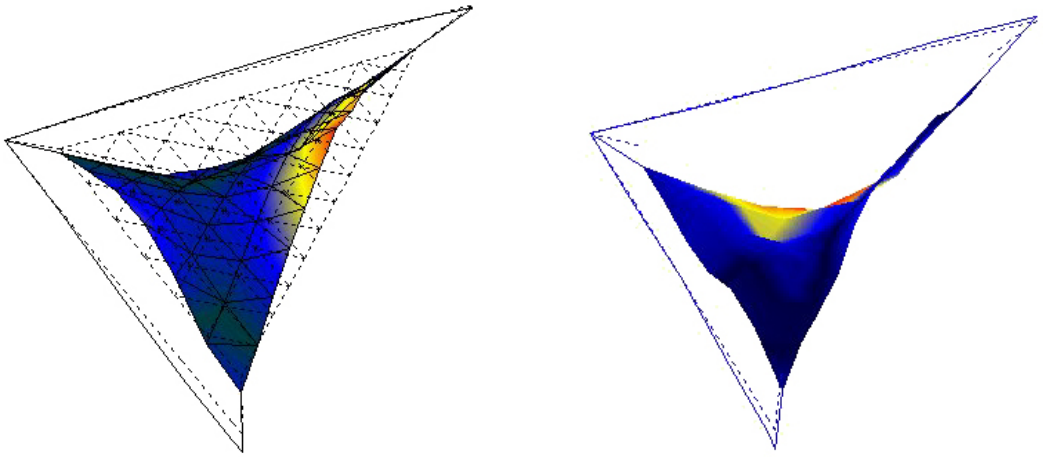

(a) 4.74 Hz Laser Vibrometer (b) 4.75 Hz Videogrammetry (FRF)

Figure 44 – Fifth deflection shape comparison for Vellum solar sail test article

The first two shapes shown in Figures 40 and 41 are basically boom driven modes. The first deflection shape shows that the booms are in phase, and the second shows the booms to be out of phase with the membrane following in a first order fashion. Figure 42 shows the third deflection shape of the system, with the booms in phase and the membrane in a second order configuration. The fourth deflection shape (Figure 43) shows the booms to be in phase with a large amplitude first order billow of the membrane. Finally, the fifth deflection shape in Figure 44 shows a saddle configuration

for the membrane. In all of the figures videogrammetry produced similar shapes at similar frequencies as the vibrometer, demonstrating the potential of the full-field non-contact dynamic characterization technique. As stated previously, videogrammetry can only measure frequencies up to approximately one half the frame rate of the cameras without hardware alterations. This limitation will not generally be a hindrance for use on gossamer structures, however, because due to their size the dominant modes will usually occur below 5.0 Hz. Also, the displacement of the test article must be large enough to be detected by the cameras, whereas the vibrometer is much more sensitive. The above results show videogrammetry to be capable, with some refinement, of achieving full-field non-contact dynamic measurements of solar sail structures.

9. CONCLUSIONS

Accurate static and dynamic characterization of solar sail test articles is vital for creating and validating high-fidelity analytical models, developing space quality hardware, and future advancement of the technology. Obtaining accurate static and dynamic measurements of the highly reflective ultra-thin membranes, however, is not a trivial task. Photogrammetry, the selected measurement method, usually relies on physically attached retro-reflective targets. The mass and stiffness these targets add to the five micron thick membranes, however, alter the static and dynamic properties the method is attempting to characterize. Therefore a totally non-contact technique called dot projection was used instead.

As with any adaptation of an established measurement method to a unique task and field, many questions arise about the accuracy of the results. Zoom lenses, color imagers, projector intensity, camera heating, highly flexible test articles, reflective object surfaces, and many other factors both complicate the measurements and affect their accuracy and resolution. Accordingly, a detailed study was performed to understand the effects of these parameters and quantify their impact on the measurement method. The three static shape applications of dot projection photogrammetry describe refinements in technique and hardware and produced noticeable gains in measurement quality from one test to the next.

9.1 Static Tests

Three experiments to statically characterize a two meter aluminized Kapton solar sail test article were performed. The first test yielded a model of the global shape of the article, but did not achieve the full accuracy or resolution potential of the dot projection

photogrammetry technique. The second test focused on a small portion of the membrane. Using the same cameras as the first test, a more powerful projector, and technique refinement, accurate modeling of surface features as small as 0.25 mm was achieved. These measurements, the first totally non-contact wrinkle characterization of solar sail membranes using photogrammetry, are of sufficient quality and resolution to be used for analytical model validation. The third and final static test used professional hardware to generate high resolution surface measurements of the entire two meter sail with an even higher quality. These tests have paved the way for other high resolution, non-contact, full-field dot projection measurements on current and future solar sail test articles and will enable the validation and refinement of analytical models that will be used to design future space missions.

9.2 Dynamic Test

Dynamic measurements were performed using an adaptation of photogrammetry to time-dependant data called videogrammetry, a method that produces a series of 3-D surface models in time. The data were exported to a modal analysis software package where two different methods were used to reduce the data and yield resonance frequencies and deflection shapes. These data were compared to data from a scanning laser vibrometer. While the videogrammetry results show good correlation to those obtained from the turn-key industrial system, they are not quite as clean, but the method is full-field and all of the data was acquired in seconds instead of the hours required by the vibrometer. The ability of the system to generate data of sufficient quality to be used for actual dynamic analysis instead of simply tracking the overall shape of the object in

time is an important breakthrough that may allow for more detailed measurements in space than previously thought possible.

9.3 Future Work

For the foreseeable future, providing high-fidelity analytical models of solar sails and other gossamer structures will be the most critical issue in the development of the technology. Static and dynamic characterization techniques that can be used reliably to provide the necessary measurement accuracy and precision for these structures are needed to validate these analytical models. Accordingly, work should continue to focus on hardware, software, and technique refinement in static measurements to achieve higher resolution on a global scale while decreasing computation time, as well as on refining the videogrammetric analysis. A detailed study must be performed to investigate thermal or other effects seen in Chapter 5. Finally, implementing a static measurement system in vacuum is necessary for future solar sail testing and for adapting the hardware for use in space.

As computers become ever faster and more powerful and prices continue to drop, consumers will have inexpensive access to capability that just a few years ago required substantial capital investment. It is foreseeable, therefore, that completely automated real time photogrammetry and videogrammetry systems could be developed and implemented for use on gossamer structures both in the laboratory and in space. Developing and implementing measurement systems that provide continuous static and dynamic data for the control systems of these structures is a realistic goal that may be achievable by the time NASA flies its first solar sail sometime before the end of the decade.

9.4 Related Work

The applications presented above represent only a portion of the work completed in this area over the past year and a half. These four applications were selected for the concise development story they tell, not for the completeness of the coverage they provide. Other work performed by the author using photogrammetry and videogrammetry includes that found in References 8, 12, 13, 24, and 38, as well as the following publications:

Black, J. T., "Photogrammetry and Videogrammetry Methods for Solar Sails and Other Gossamer Structures," *AIAA Student Conference Region I*, College Park, Maryland, April, 2003.

Leifer, J., Black, J. T., Belvin, K. W., and Behun, V., "Evaluation of Shear Compliant Boarders for Wrinkle Reduction in Thin Film Membrane Structures," *44th AIAA/ASME/ASCE/AHS/ASC Structures, Structural Dynamics and Materials Conference, 4th Gossamer Spacecraft Forum*, Norfolk, Virginia, April 2003, AIAA 2003-1984.

Johnston, J. D., Blandino, J. R., Black, J. T., and Pappa, R. S., "Structural Analysis and Testing of a 1/20th Scale NGST Sunshield Membrane Layer," *44th AIAA/ASME/ASCE/AHS/ASC Structures, Structural Dynamics and Materials Conference, 4th Gossamer Spacecraft Forum*, Norfolk, Virginia, April 2003, AIAA 2003-1742.

Photogrammetric measurements have also been taken to determine the straightness of a 7 m solar sail quality boom after a deployment in vacuum at LaRC, to determine the radial expansion of polyethylene cylinders as a function of pressure (to be published by AIAA in April 2004), to characterize the wrinkle pattern of various

configurations of horizontally supported solar sail quality membranes (to be published by AIAA in April 2004), to determine the accuracy of photogrammetry performed using various camera systems, and to measure the sag caused by gravity in a 10 m solar sail membrane quadrant under various load conditions (to be published by AIAA in April 2004).

REFERENCES

[1] Jenkins, C. H. M. (editor), *Gossamer Spacecraft: Membrane and Inflatable Structures Technology for Space Applications*, Vol. 191, Progress in Astronautics and Aeronautics, AIAA, Reston, VA, 2001.

[2] Wertz, J. R. and Larson, W. J. (editors), *Space Mission Analysis and Design*, Space Technology Library, Microcosm Press, El Segundo, CA, 1999.

[3] Chmielewski, A. B., Moore, C., and Howard, R., "The Gossamer Initiative," IEEE 0-7803-5846-5/00, 2000.

[4] Belvin, W. K., "Solar Sails: Structures and Materials Subsystem," Presentation at Technical Interchange Meeting, Structural Dynamics Branch, NASA Langley Research Center, Hampton, VA, April 2002.

[5] Nella, J., et al., "Next Generation Space Telescope (NGST) Observatory Architecture and Performance," http://www.stsci.edu/ngst/, TRW Space and Electronics / International Society for Optical Engineering (SPIE) Article, November 2002.

[6] Chmielewski, A. B., "Overview of Gossamer Structures," *Gossamer Spacecraft: Membrane and Inflatable Structures Technology for Space Applications*, Jenkings, C. H. M., ed., AIAA, Vol. 191, 2001, pp. 1-33.

[7] McInnes, C. R., *Solar Sailing – Technology, Dynamics and Mission Applications,* Praxis Publishing Ltd, Chichester, UK, 1999.

[8] Pappa, R. S., Black, J. T., and Blandino, J. R., "Photogrammetric Measurement of Gossamer Spacecraft Membrane Wrinkling," *Society for Experimental Mechanics Annual Conference*, Charlotte, NC, June 2003.

[9] Mikhail, E. M., Bethel, J. S., and McGlone, J. C., *Introduction to Modern Photogrammetry*, John Wiley & Sons, New York, NY, 2001.

[10] Pappa, R. S., Giersch, L. R., and Quagliaroli, J. M., "Photogrammetry of a 5m Inflatable Space Antenna With Consumer Digital Cameras," *Experimental Techniques*, Society for Experimental Mechanics, Vol. 25, No. 4, July/August 2001, pp. 21-29.

[11] Giersch, L. R., "Pathfinder Photogrammetry Research for Ultra-Lightweight and Inflatable Space Structures," NASA/CR-2001-211244, November 2001.

[12] Pappa, R. S., Jones, T. W., Black, J. T., Walford, A., Robson, S., and Shortis, M. R., "Photogrammetry Methodology Development for Gossamer Space Structures," *Sound and Vibration*, Vol. 36, No. 8, August 2002, pp. 12-21.

[13] Pappa, R. S., Black, J. T., Blandino, J. R., Jones, T. W., Danehy, P. M., and Dorrington, A. A., "Dot Projection Photogrammetry and Videogrammetry of Gossamer Space Structures," *Journal of Spacecraft and Rockets*, Vol. 40, No. 6, Nov.-Dec. 2003, pp. 858-867.

[14] Ganci, G., and Brown, J., "Developments in Non-Contact Measurement Using Videgorammetry," Geodetic Services, Inc., *Boeing Large Scale Metrology Seminar*, 2002.

[15] Greenwood, J. A., Darve, C., Bernstein, R., Black, E., and Kubik, D., "Failure-mode Metrology using Projected Target Videogrammetry," *Coordinate Measurement Systems Committee Conference*, Albuquerque, New Mexico, August, 2001.

[16] Gnoffo, P. A. and Anderson, B. P., "Computational Analysis of Towed Ballute Interactions," *8th AIAA/ASME Joint Thermophysics and Heat Transfer Conference*, St. Louis, Missouri, AIAA 2002-2997, 24-26 June 2002, p. 13.

[17] West, J. L. and Derbes, B., "Solar Sail Vehicle System Design for the GEOStorm Warning Mission," AIAA 2000-5326, 2000.

[18] McInnes, C. R., "Solar Sail Mission Opportunities," *Royal Astronomical Society Discussion Meeting,* 10 May 2002.

[19] Benford, G., "Assisting the Sun: Beamed Power in Space," *Aerospace America*, Vol. 41, No. 6, June 2003.

[20] Virgin, L. and Holland, D., "Post-Buckling Dynamic Structural Modeling and Analysis of Square Solar Sail Configurations," Seminar given at NASA Langley Research Center, August 2001.

[21] Hiscox, J., "Sailing to Mars," *Marsbugs: The Electronic Astrobiology Newsletter*, Vol. 9, No. 27, p. 6, 25 July 2002.

[22] Spieth, D. and Zubrin, R., "Ultra-Thin Solar Sails for Interstellar Travel – Phase I Final Report," NASA Institute for Advanced Concepts, Pioneer Astronautics Inc., December 1999.

[23] Eos Systems, Inc., *PhotoModeler Pro User's Manual*, Version 5, Vancouver, B.C., Canada, 2003.

[24] Black, J. T. and Pappa, R. S., "Videogrammetry Using Projected Circular Targets: Proof-of-Concept Test," NASA/TM-2003-212148, February 2003.

[25] Atkinson, K. B., ed., *Close Range Photogrammetry and Machine Vision*, Whittles Publishing, Caithness, Scotland, 2001.

[26] Institute of Photogrammetry, Agricultural Facility, University of Bonn, [on-line] http://www.ipb.uni-bonn.de/.

[27] Rabbani, M., "Introduction to Electronic Imaging Systems," SPIE Education Services Program, Short Course Notes, June 2002.

[28] Geodetic Services Inc., [on-line] http://www.geodetic.com/.

[29] Goldsmith, P., "Resetting the Arecibo Primary Reflector Surface," *National Astronomy and Ionosphere Center Newsletter*, Number 32, March 2001.

[30] Edmundson, K. and Baker, L., "Photogrammetric Measurement of the Arecibo Primary Reflector Surface," *Coordinate Measurement Systems Committee Conference,* Albuquerque, NM, August 2001.

[31] Avery-Dennison Corp., "Specifications for Heat Fused Durable Preformed Pavement Markings Incorporating Preapplied Visibeads, 90 Mil," 2003

[32] Golden Software, Inc., *Surfer 8 – Contouring and 3D Surface Mapping for Scientists and Engineers, User's Guide*, Golden, Colorado, 2002.

[33] Polytech, "Polytech Scanning Vibrometer Software 7.1," 2002.

[34] Polytech, "Polytech Scanning Vibrometer Theory Maual 7.1," 2002.

[35] Hardin, J. C., *Introduction to Time Series Analysis*, National Aeronautics and Space Administration, NASA RP-1145, November 1990.

[36] Batel, M., "Operational Modal Analysis – Another Way of Doing Modal Testing," *Sound and Vibration*, Vol. 36, No. 8, August 2002, pp. 22-27.

[37] Vibrant Technology, Inc., *ME'scope VES, Visual Engineering System, Operating Manual*, Jamestown, CA, 2001.

[38] Blandino, J. R., Pappa, R. S., and Black J. T., "Modal Identification of Membrane Structures with Videogrammetry and Laser Vibrometry," *44th AIAA/ASME/ASCE/AHS/ASC Structures, Structural Dynamics and Materials Conference, 4th Gossamer Spacecraft Forum*, Norfolk, VA, AIAA Paper 2003-1745, April 2003.

[39] Ewins, D. J., *Modal Testing: Theory and Practice*, John Wiley & Sons Inc., New York, NY, 1984.

APPENDIX A – CALIBRATION TRACKING

Calibrating the cameras used in the photogrammetric process is vital to achieving accurate measurements. The parameters listed in Tables A-1 and A-2 were obtained from calibrations performed on the dates listed and are as follows: Focal Length is the exact zoom setting of the camera, Format Size is the exact size of the CCD imager, Format Ratio is the Format Width divided by the Format Height, Principal Point coordinates are the exact center of the image on the CCD, and K1, K2, P1, and P2 are the radial and descentering lens distortion parameters, all of which are described in detail in Section 3.2.1. Table A-3 shows estimates of the radial distortion for one Olympus camera and one Kodak camera calculated using the constants in Tables A-1 and A-2 and Equations 1-5 in Section 3.2.1.

Tables A-1 and A-2 show that over time small changes in the calibration parameters do occur. These changes can be caused by a number of factors, including repeated use, settling of the lenses and internal camera components, vibrations, thermal warping, etc. It is important to note that while maintaining up-to-date calibrations of all of the cameras is vital to attaining maximum accuracy in photogrammetric measurements, the observable deviations in all of the parameters listed below do not follow any predictable pattern which may indicate a systemic flaw. The parameters vary over time by less than ten percent.

Table A-1 – Calibration parameters for Olympus E20n cameras

Camera	Date	Focal Length (mm)	Format Size W (mm)	Format Size H (mm)	Format Ratio (W/H)	Principal Point X (mm)	Principal Point Y (mm)
1	Jan-02	9.1599	8.7042	6.5280	1.3334	4.3821	3.1998
	Jul-02	9.1930	8.7004	6.5280	1.3328	4.3805	3.1900
	Nov-02 vac	9.1782	8.7088	6.5280	1.3341	4.3672	3.1850
	May-03	9.0775	8.6201	6.4660	1.3331	4.3077	3.1640

	Jan-02	9.1611	8.7082	6.5280	1.3340	4.3454	3.1578
2	Jul-02	9.1978	8.7060	6.5280	1.3336	4.3317	3.1427
	Nov-02 vac	9.1936	8.7119	6.5280	1.3345	4.3328	3.1361
	Jan-02	9.1732	8.7059	6.5280	1.3336	4.3454	3.1793
3	Nov-02 vac	9.1835	8.7093	6.5280	1.3341	4.3321	3.1613
	May-03	9.0035	8.5555	6.4179	1.3331	4.2349	3.1145
	Jan-02	9.1294	8.7019	6.5280	1.3330	4.2313	3.2346
4	May-03	8.1852	7.7838	5.8382	1.3333	3.7613	2.8928
	Jan-02	9.1733	8.7078	6.5280	1.3339	4.3921	3.1654
5	Jul-02	9.1795	8.7086	6.5280	1.3340	4.3814	3.1627
	Nov-02 vac	9.1628	8.7150	6.5280	1.3350	4.3844	3.1528
6	Jul-02	9.1690	8.7075	6.5280	1.3339	4.3255	3.1988

Camera	Date	K1	K2	P1	P2
	Jan-02	0.002235	-1.491E-05	-2.682E-05	6.639E-05
	Jul-02	0.002487	-2.537E-05	-7.780E-05	1.428E-05
1	Nov-02 vac	0.002476	-2.270E-05	-2.183E-05	6.675E-05
	May-03	0.002521	-2.383E-05	3.316E-05	1.209E-05
	Jan-02	0.002473	-1.529E-05	2.084E-05	3.185E-05
2	Jul-02	0.002593	-2.829E-05	-1.264E-05	1.862E-05
	Nov-02 vac	0.002421	-2.311E-05	-1.518E-08	3.918E-05
	Jan-02	0.002376	-2.271E-05	6.969E-06	4.028E-06
3	Nov-02 vac	0.002466	-2.475E-05	7.917E-06	6.676E-05
	May-03	0.002446	-2.260E-05	8.106E-05	-9.308E-06
	Jan-02	0.002393	-2.847E-05	-5.028E-06	-2.549E-05
4	May-03	0.003092	-3.779E-05	1.070E-04	3.949E-05
	Jan-02	0.002467	-2.663E-05	-8.715E-05	1.023E-05
5	Jul-02	0.002519	-2.704E-05	-2.521E-05	-1.937E-06
	Nov-02 vac	0.002582	-2.945E-05	2.317E-05	3.463E-05
6	Jul-02	0.002475	-2.446E-05	-8.344E-05	-5.966E-05

vac = in early November 2002 these cameras were used in vacuum chamber tests and were calibrated immediately thereafter

Table A-2 – Calibration parameters for Kodak DCS 760M cameras

Camera	Date	Focal Length (mm)	Format Size W (mm)	Format Size H (mm)	Format Ratio (W/H)	Principal Point X (mm)	Principal Point Y (mm)
	Oct-02 4.0	24.2855	27.2391	18.0000	1.5133	13.7492	9.1606
155	Feb-03	23.7714	26.6274	17.6116	1.5119	13.4723	8.9743
	May-03	23.9696	26.8440	17.7549	1.5119	13.6199	9.0644
	Mar-03	23.3584	26.2020	17.3344	1.5116	13.3156	8.7496
156	May-03	23.9087	26.8387	17.7563	1.5115	13.6591	8.9651
	Apr-03	23.7165	26.6078	17.5997	1.5118	13.4136	8.9274
159	May-03	24.0166	26.9576	17.8314	1.5118	13.5825	9.0585
	Apr-03	23.9109	26.8404	17.7472	1.5124	13.6499	9.0456
163	May-03	24.0115	26.9594	17.8272	1.5123	13.7150	9.0823

Camera	Date	K1	K2	P1	P2
	Oct-02 4.0	0.0001634	-2.670E-07	-2.710E-05	2.273E-05
155	Feb-03	0.0001717	-2.697E-07	-3.332E-05	2.844E-06
	May-03	0.0001679	-2.604E-07	-3.510E-05	2.237E-06
	Mar-03	0.0001797	-2.919E-07	-2.256E-05	-1.352E-05
156	May-03	0.0001718	-2.680E-07	-2.715E-05	-1.228E-05
	Apr-03	0.0001726	-2.780E-07	-6.645E-06	9.491E-07
159	May-03	0.0001681	-2.645E-07	-5.885E-06	1.700E-06
	Apr-03	0.0001676	-2.649E-07	-3.301E-06	-7.875E-06
163	May-03	0.0001666	-2.621E-07	-3.200E-06	-8.613E-06

4.0 = release 4.0 of the photogrammetry software. Other calibrations from release 5.0.

Table A-3 – Residual estimates for one Olympus E20n and one Kodak DCS 760M

Radial Distance, r (mm)	E20 δr (mm)	E20 δr_x (mm)	E20 δr_y (mm)	760M δr (mm)	760M δr_x (mm)	760M δr_y (mm)
1	2.497E-03	1.888E-03	1.635E-03	1.676E-04	1.301E-04	1.009E-04
2	1.941E-02	1.467E-02	1.270E-02	1.335E-03	1.036E-03	8.035E-04
3	6.228E-02	4.708E-02	4.077E-02	4.470E-03	3.468E-03	2.690E-03
4	1.369E-01	1.035E-01	8.965E-02	1.048E-02	8.130E-03	6.307E-03
5	2.407E-01	1.819E-01	1.576E-01	2.017E-02	1.565E-02	1.214E-02
	Max Magnitude (mm) =		2.407E-01			2.017E-02

REPORT DOCUMENTATION PAGE

Form Approved
OMB No. 0704-0188

1. REPORT DATE *(DD-MM-YYYY)*	2. REPORT TYPE	3. DATES COVERED *(From - To)*
01- 12 - 2003	Contractor Report	

4. TITLE AND SUBTITLE

Photogrammetry and Videogrammetry Methods Development for Solar Sail Structures

5a. CONTRACT NUMBER

NCC1-03008

5b. GRANT NUMBER

5c. PROGRAM ELEMENT NUMBER

6. AUTHOR(S)

Black, Jonathan T.

5d. PROJECT NUMBER

5e. TASK NUMBER

5f. WORK UNIT NUMBER

23-629-80-01

7. PERFORMING ORGANIZATION NAME(S) AND ADDRESS(ES)

NASA Langley Research Center
Hampton, VA 23681-2199

8. PERFORMING ORGANIZATION REPORT NUMBER

9. SPONSORING/MONITORING AGENCY NAME(S) AND ADDRESS(ES)

National Aeronautics and Space Administration
Washington, DC 20546-0001

10. SPONSOR/MONITOR'S ACRONYM(S)

NASA

11. SPONSOR/MONITOR'S REPORT NUMBER(S)

NASA/CR-2003-212678

12. DISTRIBUTION/AVAILABILITY STATEMENT

Unclassified - Unlimited
Subject Category 39
Availability: NASA CASI (301) 621-0390 Distribution: Standard

13. SUPPLEMENTARY NOTES

Thesis submitted to the faculty of The School of Engineering and Applied Science of The George Washington University in partial satisfaction of the requirements for the degree of Master of Science, August 29, 2003.
An electronic version can be found at http://techreports.larc.nasa.gov/ltrs/ or http://ntrs.nasa.gov. Technical Monitor: Richard S. Pappa

14. ABSTRACT

This report discusses the development and application of metrology methods called photogrammetry and videogrammetry that make accurate measurements from photographs. These methods have been adapted for the static and dynamic characterization of gossamer structures, as four specific solar sail applications demonstrate. The applications prove that high-resolution, full-field, non-contact static measurements of solar sails using dot projection photogrammetry are possible as well as full-field, non-contact, dynamic characterization using dot projection videogrammetry. The accuracy of the measurement of the resonant frequencies and operating deflection shapes that were extracted surpassed expectations. While other non-contact measurement methods exist, they are not full-field and require significantly more time to take data.

15. SUBJECT TERMS

Photogrammetry; Videogrammetry; Optical measurement techniques; Dot projection; Solar sails; Gossamer spacecraft; Structural test methods

16. SECURITY CLASSIFICATION OF:			17. LIMITATION OF ABSTRACT	18. NUMBER OF PAGES	19a. NAME OF RESPONSIBLE PERSON
a. REPORT	b. ABSTRACT	c. THIS PAGE			STI Help Desk (email: help@sti.nasa.gov)
					19b. TELEPHONE NUMBER *(Include area code)*
U	U	U	UU	102	(301) 621-0390